5

Bunch Compressors and Prelinac

Contents

5.1 Introduction

This chapter describes the NLC bunch compressors, which compress the 4-mm-long bunches from the damping rings to the $100 \sim$150-μm bunch lengths required in the main linacs and final foci. It also describes the S-band prelinacs that accelerate the beams from the damping rings at roughly 2 GeV to an energy of 10 GeV and the spin rotators that provide control over the particle spin orientation. These systems are part of the low-energy injector complex that prepares the beams for injection into the X-band main linacs. Thus, it is essential that they provide a stable and reliable platform for the tuning of the linacs and final foci. In the next paragraphs, we briefly summarize the status of each of these subsystems before delving into greater detail in the body of the chapter.

The first items in the compressor systems are the spin rotators which are located at the exit of the damping rings. We plan to install a spin rotator on the electron side and leave space for an installation on the positron side. This is to allow for a future upgrade to polarized positrons or polarized electrons which would be wanted for γ-γ or e^--e^- collisions. The rotators are based on pairs of solenoids separated by a horizontal arc to allow full control over the spin orientation; this is similar in concept to the original SLC spin rotator system. Solenoids were chosen to control the spin because the other alternate, namely a snake, requires a vertical bending chicane which must be unreasonably long to prevent synchrotron radiation from increasing the vertical emittance. Of course, the problem with solenoids is that they couple the beam which, with flat beams, leads to an increase in the projected vertical emittance; this is the reason the original solenoid system is not presently used in the SLC. Our present design uses pairs of solenoids which are optically separated so that the coupling is fully canceled. There are very tight tolerances on the quadrupole fields between the sextupoles but an extensive skew correction system has been included to ease the tolerances as well as correct any residual coupling from the damping rings.

Next, the NLC bunch compressors must compress the bunches from the damping rings with 4-mm lengths to the $100 \sim$150-μm bunch lengths required in the main linacs and final foci. To perform the compressions, a two-stage compressor system has been designed: the first stage follows the damping rings and the second stage operates at a beam energy of 10 GeV at the exit of the 8-GeV S-band prelinacs.

The two-stage system has a number of advantages over a single stage compressor. In particular, it keeps the rms energy spread less than roughly 2%, it is optically more straightforward, and the bunch lengths are more logically matched to the acceleration rf frequency so that the energy spread due to the longitudinal wakefields can be canceled locally. The disadvantage of the two-stage design is that it is more complex and lengthy than a single-stage compressor. The first stage rotates the longitudinal phase by $\pi/2$ while the second stage performs a 2π rotation. In this manner, phase errors due to the beam loading in the damping rings and energy errors due to imperfect multibunch energy compensation in the 8-GeV S-band prelinacs do not affect the beam phase at injection into the main linac.

One of the driving philosophies behind the NLC compressor design has been to utilize naturally achromatic magnetic lattices wherever the beam energy spread is large. In particular, the optics is chosen so that quadrupoles are not placed in regions of large dispersion and strong sextupoles are not needed. This choice arises from experience with the SLC bunch compressors which are based on second-order achromats where quadrupoles are located in dispersive regions and strong sextupoles are used to cancel the chromatic aberrations. Unfortunately, the SLC design is extremely difficult to operate and tune because of the large nonlinearities and the sensitivity to multipole errors in the quadrupoles; over the years additional nonlinear elements have been added (skew sextupoles and octupoles) to help cancel the residual aberrations but the tuning is still difficult. To further facilitate the tuning in the NLC design, we have explicitly designed orthogonal tuning controls and diagnostics into the system. We feel confident that these considerations will make the system relatively straightforward to operate and tune.

Finally, the rf acceleration throughout the compressor system, *i.e.*, the bunch compressor rf and the 8-GeV prelinac, is performed with relatively low frequency rf. In particular, the first bunch compressors use L-band (1.4 GHz) rf and the prelinac and second bunch compressor use S-band (2.8 GHz) acceleration. Although these systems are, in general,

longer and more expensive than higher frequency accelerator systems, we feel that they are needed at the low beam energy. In particular, we have designed the systems so that they have small beam loading and relatively loose alignment tolerances. This is important to provide the reliability and stability that is desired in the bunch compressor system. Of course, such lightly-loaded systems are inefficient and could not be used to accelerate the beams to very high energy.

To minimize the long-range transverse wakefields, all of the accelerator structures are Damped-Detuned Structures (DDS), similar to those developed for the X-band main linacs. In addition, the beam loading is primarily compensated using the ΔT (early injection) method. This has the advantage of canceling the bunch-to-bunch energy deviations locally within an accelerator structure thereby minimizing the transverse emittance growth due to dispersive and chromatic effects. Details of the multibunch beam loading compensation, the accelerator structures, and power sources is presented in Chapter 6.

The design described in this chapter appears to meet, or even to surpass, all requirements; the requirements are detailed in Section 5.2. At the same time, the present design still allows for improvements and optimization. First, because the designs were being made concurrently, we overestimated the errors in the beams from the damping rings that we should expect—assuming a more reasonable input beam could significantly change the optimization and potentially decrease the length and complexity of the compressor system. Second, an option of simplifying the second stage to only perform a $\pi/2$ rotation in longitudinal phase space should be explored. This also could provide a substantial saving in length and S-band rf components, but it will require tighter tolerances on the phase variation in the damping rings and the energy compensation in the 8-GeV S-band prelinac. Third, another path, that should be further investigated, is the possibility of optically compensating the longitudinal nonlinearities. The present design uses additional rf systems in the second compressor to compensate the longitudinal nonlinearities introduced in the dispersive regions. It would certainly be desirable to compensate these effects locally without having to resort to the additional rf systems.

In the next section (Section 5.2), we review the requirements of the system and the assumed beam from the damping ring. We then provide an overview of the design choices that were made and some of the alternate options. Next, in Section 5.3, we describe the various components of the compressor in more detail and in Sections 5.4 and 5.5, we discuss the longitudinal and transverse dynamics which are relevant to the design, and the tuning schemes that are needed to attain the desired performance. The tolerances and tuning schemes are described in Section 5.6, and the chapter concludes with a summary and an outlook on further studies.

Finally, it should be noted that, at the time of this study, not all of the damping ring or the low frequency rf system parameters were finalized. Thus, in many of the dynamics studies, performed for the bunch compressors, we intentionally over-estimated the expected errors to provide a margin. The example of the synchronous phase offsets has already been mentioned. Similarly, we assumed SLAC S-band wakefields when calculating effects of the accelerator structures. Because the present design calls for structures that have roughly twice the group velocity, the SLAC transverse single bunch wakefield is roughly a factor of two too strong and the longitudinal wakefield is roughly a factor of $\sqrt{2}$ too strong. Thus, the system will perform even better than has been calculated. We will note sections that have these errors.

5.2 Requirements and Design Options

In this section, we will describe the design goals of the bunch compressor systems and beam requirements. We will also outline the design choices that were made and some of the alternate options.

5.2.1 Design Goals

The NLC bunch compressor system is designed with six goals:

- The compressor system must compress a bunch with $\sigma_z \approx 4$ mm from the damping rings to the $\sigma_z = 100\ \mu$m $\sim$ $150\ \mu$m needed in the main X-band linacs and the final foci. This requires compressing the bunch length, and correspondingly increasing the energy spread, by a factor of 30–40.
- The bunch compressor system should be able to compensate for bunch-to-bunch phase offsets induced by the beam loading in the damping rings; if not corrected, these phase errors would become energy errors at the end of the linacs. This requires that the compressor system rotate the longitudinal phase space by $\pi/2$, translating the phase errors into injection energy errors.
- The bunch compressor system should provide a trombone-like arm, reversing the direction of the beam before injection into the main X-band linacs. This allows extension of the linac lengths to upgrade the beam energy at the IP without significant modification to the injection systems. It also allows for abort systems to dump the beam and feed-forward systems to correct the beam trajectory, phase, and energy before injection into the main linacs.
- The compressor system must include a spin rotator system that can rotate the polarization vector of the electron beam from the vertical plane to any arbitrary orientation. This is easiest at lower beam energy.
- The compressor system must be able to correct for coupling mismatches from the damping rings; dispersive mismatches from the damping rings will be corrected in the ring extraction line, described in Chapter 4.
- The compressor systems are the injectors into the main linac and they need to provide a stable and reliable platform to allow tuning of the linac and final focus systems. The system should have reasonable tolerances and limit the horizontal and vertical emittance dilutions to 20% and 30% respectively.

5.2.2 Beam Requirements

In this section, we describe the injected and extracted beam requirements; these are summarized in Table 5-1. The damping rings are designed to produce beams with a relative energy spread of $\sigma_\delta \sim 1 \times 10^{-3}$ and a bunch length of $\sigma_z \approx 4$ mm. The beam emittances are damped to $\gamma\epsilon_x = 3 \times 10^{-6}$ m-rad and $\gamma\epsilon_y = 3 \times 10^{-8}$ m-rad and the spin is oriented vertically to preserve the polarization in the rings.

The compressor system has been designed to accept beams whose incoming phase varies due to the transient beam loading in the damping rings. The present design allows for phase errors of $\pm$20 ps while limiting the phase error of the extracted beams to less than $\pm 0.2^\circ$ of X-band. This will limit the resulting energy error at the end of the main linac to less than 0.1% and will limit the luminosity loss due to shifts of the collision point to less than 1%. It should be noted that, in the present damping ring design, the phase variation is less than ± 12 ps (Chapter 4).

The compressor system will operate with a train of 90 bunches having bunch charges of 0.68×10^{10} particles for NLC-Ia and 1.31×10^{10} particles for NLC-IIc; these values are 5% higher than the design bunch charges at the IP to provide overhead in the bunch charge. The higher charge for NLC-IIc coincides with longer bunches in the main linacs ($\sigma_z = 150\ \mu$m) while the lower charge in NLC-Ia corresponds to a shorter bunch length (100 μm).

In all cases, the expected beam loss through the compressor system is much less than 1%. To provide an additional margin, the compressor system has been designed to accept beams with an initial bunch length of 5 mm. Because

Inj. Energy	1.8–2.2 GeV
Inj. Bunch charge/Beam current	$< 1.31 \times 10^{10} / < 1.5$ A
Inj. Phase error Δz	< 6 mm (4 mm expected)
Inj. Bunch length σ_z	< 5 mm (4 mm expected)
Inj. Energy error $\Delta E/E$	$< 0.01\%$
Inj. Energy spread σ_δ	0.1%
Inj. Emittances $\gamma\epsilon_x$, $\gamma\epsilon_y$	$3 \times 10^{-6}, 3 \times 10^{-8}$
Ext. Energy	10 GeV
Charge loss	$< 1\%$
Ext. Phase error Δz	< 15 μm
Ext. Bunch length σ_z	$100 - 150$ μm
Ext. Energy error $\Delta E/E$	$< 3\%$
Ext. Energy spread σ_δ	$< 1.5\%$
Ext. Emittances $\gamma\epsilon_x$, $\gamma\epsilon_y$	$3.6 \times 10^{-6}, 4 \times 10^{-8}$

Table 5-1. *Input and extracted beam requirements for compressor system.*

there are no quadrupoles in regions of large dispersion, this has minimal impact on the design requiring only slightly larger horizontal apertures in the bending magnets and vacuum system. All apertures have been specified in excess of $\pm 5\sigma_{x,y}$ plus an allowance for the injected phase error of ± 6 mm and an additional allowance for steering errors of 2 mm; the allowance of 2 mm for steering errors is based on present SLC operation.

Finally, the bunch compressor system has been designed to have minimal emittance dilutions. In particular, the system needs to limit the horizontal emittance dilution to 20% and the vertical dilution to 30% while providing a stable platform for the tuning of the downstream systems. Wherever possible we have chosen technologies that, while more expensive or less efficient, will ease the tolerances. We believe the added cost and inefficiency is acceptable for these relatively small sections.

5.2.3 Spin Rotator Options

The spin rotator system must orient the spin so that the polarization is longitudinal at the IP. Because there is net bending in the collider to provide for the multiple IPs with a 20-mr crossing angle and because the beam energy at the IPs will be varied, it is necessary to provide full control over the orientation of the spin vector. To control the orientation of the spin vector, one can either use solenoids or a snake or serpent design that consists of interleaved horizontal and vertical bending magnets.

The choice of a rotator system is determined by emittance dilution constraints and limitations on the momentum compaction (R_{56}). In the NLC, it would be difficult to preserve the vertical emittance of $\gamma\epsilon_y = 3 \times 10^{-8}$ m-rad through a "half-serpent" system [Fieguth 1987] which necessarily includes vertical bending. To limit the vertical emittance dilution due to synchrotron radiation to 2%, one can show that the length of the vertical dipole magnets is related to the beam energy as [Emma 1994].

$$L[\text{m}] > 190 E[\text{GeV}] \quad . \tag{5.1}$$

Even at the minimum beam energy of 2 GeV, the bending magnets must become excessively long. For this reason, a solenoid-based rotator system was chosen. It is located immediately after damping ring extraction where the beam

energy is low and the beam energy spread is small. The betatron coupling introduced by the solenoids is corrected by using pairs of solenoids separated by an optical transformation so that the coupling is canceled.

5.2.4 Bunch Compressor Options

For the NLC design, we are currently planning to use a two-stage compressor design which is outlined in Ref. [Raubenheimer 1993]. The first stage, located after the spin rotator, compresses the bunch from the damping rings to $\sigma_z = 500\ \mu$m for injection into an S-band prelinac. There, the beam is accelerated from the damping ring energy of roughly 2 GeV to an energy of 10 GeV where it is injected into the second stage of the compressor. This second stage compresses the bunch to the final bunch length of $\sigma_z = 100\ \mu$m–$150\ \mu$m, before injection into the X-band main linac. The first compressor stage rotates the phase space by roughly $\pi/2$ and the second stage rotates the longitudinal phase space by 2π so that the beam phase in the X-band main linac is independent of the phase in the damping rings.

While the linear design of such a two-stage bunch compressor system is conceptually straightforward, the design is complicated by the large longitudinal nonlinearities introduced in both the bending sections and the rf sections. The solution we have adopted is to use the nonlinearity of an additional sinusoidal rf to cancel the nonlinearity introduced in the bending sections, but this is difficult and is potentially dangerous; systems where one large effect cancels another large effect are inherently extremely sensitive. We have investigated some options of decreasing the optical longitudinal nonlinearities by adding sextupoles but these made the transverse phase space unacceptable. These issues will be discussed further in Section 5.4.

Alternate Approaches

Unfortunately, the second-stage bunch compressor is complicated because of the required 2π rotation in longitudinal phase space. One possible alternate approach would be to use a $\pi/2$ compressor for the second stage *if the S-band linac can be used to compensate the bunch-to-bunch energy deviations*. This would have two advantages: first, it simplifies the design of the second stage compressor; the required R_{56} (the R_{56} is the (5,6) element in the linear transfer matrix) in the second compressor would be 0.05 m which would be easily achieved with a simple FODO arc. Second, such a system might allow one to tune the bunch-to-bunch energy deviation of the beam after the X-band linac by making small phase changes in the second compressor. The allowable phase changes must be small compared to the final beta function of $100\ \mu$m, *i.e.*, $\Delta\phi \ll 1^\circ$ X-band.

It is also possible to consider designing a single-stage bunch compressor system at the exit of the damping rings, but the large energy spreads and large space charge forces at the exit of the compressor are thought to make preservation of the transverse emittances difficult; a systematic study of the required tolerances has not been performed. In addition, the nonlinearity in the longitudinal phase space would seem to complicate if not preclude this option (see the discussion in the next section).

Alternatively, one could consider accelerating the uncompressed beam from the damping rings in a low-frequency structure and then use a single-stage compressor. This option would reduce the relative energy spread and the space charge forces, but, because of the nonlinearity of both the rf and the T_{566}, it is more difficult to perform the 90° rotation. This system does not appear to have significant advantages over the present design and thus we will not consider it further.

Single-Stage *vs.* **Multistage**

At first glance, a single-stage compressor has several advantages compared with the two-stage solution. It is simpler, contains less elements, and, perhaps most importantly, avoids the significant wakefield effects in the prelinac, thereby improving the longitudinal dynamics at high intensity. It has also been argued that a single-stage compressor may ease the compensation of multibunch effects [Oide 1994].

The main disadvantages of a single-stage compressor are the increase of the final energy spread to 5%, which enhances the harmful effects of the T_{566} and U_{5666} and the much larger sensitivity to incoming phase variations; the T_{566} and U_{5666} are the TRANSPORT notation for the higher-order dependences of the path length on the energy deviation: z-δ^2 and z-δ^3. The nonlinearity of the rf alone is already significant. Assuming an L-band rf system, an initial phase error $z_0 \approx \sigma_{z0} \approx 5$ mm would change the final phase at the exit of the compressor by $\Delta z_f \approx k^2 z_0^3/6 \approx 20\,\mu$m, where, as before, $k \equiv 2\pi/\lambda$. Such a change is too large to be tolerable, considering that the beam in the main linac will be off crest by about 10–15° and that the energy change at the end of the linac has to be small.

As a concrete example, we have performed simulations of the longitudinal dynamics for a single compressor consisting of 750-MV L-band rf and a wiggler (or chicane) with $R_{56} \approx 9$ cm. In the ideal case of perfectly compensated U_{5666} and T_{566}, an initial phase error of ± 6 mm increases the final bunch length to 155 μm (from 100 μm for no initial phase offset). If the T_{566} is included, without compensation, the final rms bunch length for zero initial phase error is as large as 58 mm. Applying a compensating S-band rf, as discussed for the double-stage compressor, the minimum final bunch length as a function of compensating voltage V_c was found to be 400 μm, for $V_c \approx 195$ MV and no initial phase error. Such a single-stage compressor does not fulfill our specifications.

To make a single-stage compressor a viable and attractive option, the T_{566}-matrix-element has to be smaller than about a third of the R_{56}-matrix-element (for a generic wiggler or chicane, $|T_{566}|$ is 1.5 times R_{56}). If the T_{566}-matrix-element is of this size, the residual nonlinearity can be compensated by a decelerating rf as in the double-stage scheme, without introducing other intolerable aberrations. A small T_{566}-matrix-element may be realized by manipulating the second-order dispersion via quadrupoles at dispersive locations and/or via additional sextupoles. A further complication arises, however, in the transverse phase space, where dilutions of the transverse emittance have to remain tolerable for an rms energy spread as large as 5%. These two requirements, small T_{566} and tolerable transverse emittance dilution, appear to be in conflict with each other, as changes to the second-order dispersion also generate higher-order dispersion and chromaticity, which affect the transverse emittances.

For these reasons, attempts to design a single-stage compressor with satisfactory performance in all phase-space dimensions have not yet been successful.

5.2.5 RF Frequency Choices

The choice of rf frequency depends upon the bunch length and the expected phase variations from the damping rings, the sensitivity to multibunch beam loading, the alignment tolerances, and the length and cost of the rf system. The tolerances due to all of these effects are significantly eased by using lower rf frequency with lightly beam-loaded structures. The disadvantage of lower-frequency rf is the system cost and poorer efficiency.

For example, in the low-energy compressor, one can use 139 MV of L-band rf, which requires roughly 10 m of accelerator structure, or 70 MV of S-band rf which could be provided with roughly 3 m of accelerator structure. But, the multibunch loading is more difficult to compensate in the S-band system and would require using the ΔF compensation technique. Therefore, we would need three different structures with slightly different rf frequencies and three klystrons to power the structures. Furthermore, for the same transverse emittance dilution, the transverse alignment tolerances on the S-band structure are more than five times tighter than on the L-band structures. Since

the bunches are long in the bunch compressors the alignment tolerances are tight anyway and the factor of five is significant. For these reasons and because the additional cost is not a significant limitation in these short rf sections, the present design is based on the lower-frequency rf systems. In particular, we use L-band rf (1.4 GHz) in the low-energy compressors and S-band rf (2.8 GHz) in the prelinacs and the high-energy compressors.

In all cases, we will use Damped-Detuned Structures similar to those developed for the X-band main linacs. These minimize the long-range transverse wakefields as well as provide a straightforward method of measuring the induced dipole modes which are used to align the structures to the beam. The structures, power sources, rf pulse compressors, and details of the beam-loading compensation are all described in Chapter 6.

5.2.6 Tuning and Diagnostics

Although the tolerances on components in the bunch compressor systems are not nearly as tight as in the main linacs or the final foci, we have chosen to adopt the same methods of beam-based alignment and tuning. In particular, to ease the alignment procedures, all of the quadrupoles will be mounted on remote magnet movers and will be powered by individual power supplies. In addition, each quadrupole will contain a BPM with a resolution of $1\ \mu$m. Similarly, all of the accelerator structures will be instrumented with an rf BPM to measure the induced dipole modes and each girder will be remotely movable; depending on location, the girders will support either one or two structures. All of these components: the $1\ \mu$m resolution BPMs, the magnet and structure movers, and the structure BPMs, are described in Chapter 7 which discusses the design of the main X-band linacs.

Finally, there are three emittance diagnostic stations located through each compressor system: one after the low-energy compressor, one after the prelinac, and one after the high-energy bunch compressor. Each diagnostic station will contain four laser wire scanners so that emittance measurements can be made without disrupting the collider operation. Lastly, there will be a pulsed beam dump after each diagnostic station so that the various subsystems can be tuned before sending the beams further downstream.

5.3 System Design

In this section, we will describe the present design of the bunch compressor system. We start with a description of the overall layout and then describe the various subsystems in sequence. A discussion of the longitudinal and transverse dynamics in the compressor system can be found in Sections 5.4 and 5.5, respectively. Finally, the system tolerances are discussed in Section 5.6.

5.3.1 Layout

The bunch compressor system starts at the end of the extraction lines from the main damping rings where the beam energy is between 1.8 and 2.2 GeV. It includes the matching and spin rotation sections, the first bunch compressor, and subsequent diagnostics. It also includes the S-band prelinac that accelerates the beam from roughly 2 GeV to 10 GeV. Finally, it includes the second bunch compression system which contains a 180° arc, a compressor rf section, a chicane, and the matching and diagnostics beyond the end of the chicane for injection into the main linac. The compressor system also includes three pulsed beam dumps to allow tuning of the various subsystems before taking the beam further down the collider.

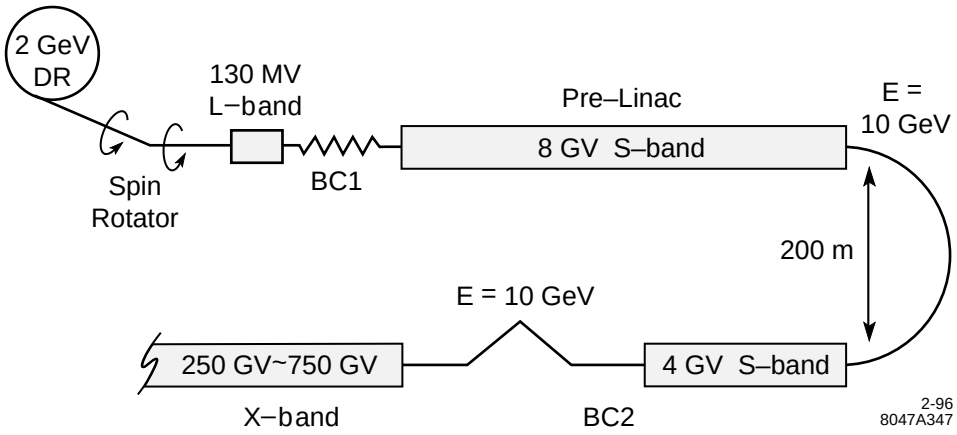

Figure 5-1. *Schematic of the NLC bunch compressor system.*

The length of the spin rotator and first bunch compressor is roughly 170 m while the prelinac is roughly 450-m long. Finally, the 180° arc is roughly 330 m and the second compressor rf and chicane are 350-m long. Thus, the overall system is 1.3 km in length. A schematic view is given in Figure 5-1.

5.3.2 Ring Extraction

The beams are extracted from the main damping rings using an achromatic kicker system and achromatic extraction septum. These are described in Chapter 4 and the component layout is illustrated in Figure 4-14. The bunch compressor beam line begins after the compensation kicker. It starts with six quadrupoles to match the lattice functions into the spin rotator system. A single laser wire scanner is included in this section to provide a continuous diagnostic on the ring performance and quad-scan emittance measurements when necessary. This wire will be used to verify the beta match and minimize any residual dispersion leaking from the damping ring. Finally, there will be a fast-feedback system to control the extraction positions and angles from the damping rings. Similar feedback systems are used in many places through the SLC and are described in Appendix D.

5.3.3 Spin Rotator

The spin rotator system is located immediately after the damping rings. It consists of four paired superconducting solenoids and an intermediate short arc that bends the beam by roughly 20°. The system is designed to operate over the energy range of 1.8 GeV–2.2 GeV. At the nominal energy of 2 GeV, it allows complete control over the spin orientation; at other energies, some of the tuning range is lost but it should still be sufficient. The betatron coupling introduced by the solenoids is canceled by using pairs of solenoids separated by an I transform in X and a $-I$ transform in Y. Although such a cancelation system is sensitive to errors, tuning simulations show that it is straightforward to correct the system; the tuning studies are described in Section 5.5. In this section, we describe the rotator optical design and performance.

Cross-plane Coupling Compensation in a Solenoid Rotator

Solenoid magnets can be implemented to rotate the electron spin about the longitudinal axis by ψ; however, they radially focus the beam and unfortunately introduce a roll about the beam axis [Fieguth 1989]. The damped, flat beam is rolled through an angle ψ_b, which is roughly one-half that of the spin precession.

$$\psi_s = \left[1 - \left(\frac{g-2}{2}\right)\right] \frac{B_z L_s}{(B_0\rho)} \approx \frac{B_z L_s}{(B_0\rho)} = 2\psi_b \tag{5.2}$$

In Eq. 5.2, L_s is the effective solenoid length, B_z is the longitudinal magnetic field and $(B_0\rho)$ is the usual magnetic rigidity. For electrons, $(g-2)/2 \approx 1.16 \times 10^{-3}$, is the anomalous magnetic moment and can be ignored. The large $x-y$ coupling introduced when passing the solenoid can potentially destroy the vertical emittance. It can be shown that the vertical projected emittance at the end of a solenoid of strength ψ_s is

$$\epsilon_y^2 = \epsilon_{x_0}^2 S^4 + \epsilon_{y_0}^2 C^4 + \epsilon_{x_0}\epsilon_{y_0} C^2 S^2 \left(\beta_x\gamma_y - 2\alpha_x\alpha_y + \beta_y\gamma_x\right) \quad , \tag{5.3}$$

where $C \equiv \cos(\psi_s/2)$, $S \equiv \sin(\psi_s/2)$, and $\beta_{x,y}, \alpha_{x,y}, \gamma_{x,y}, \epsilon_{x_0,y_0}$ are the beam Twiss parameters and initial emittances at the solenoid entrance. For $\psi_s = \pi/2$, equal Twiss parameters in the two planes and a horizontal-to-vertical emittance ratio of 100 as in the NLC, the vertical emittance after the solenoid increases as

$$\frac{\epsilon_y}{\epsilon_{y_0}} = \frac{\epsilon_{x_0}}{\epsilon_{y_0}} S^2 + C^2 \approx 50 \quad . \tag{5.4}$$

A coupling compensation system needs to be included which is able to reliably correct this large emittance increase. A system of skew quads can be imagined but has the undesirable character of requiring new skew quad settings for each new solenoid setting. A more robust correction scheme can be designed by splitting the solenoid in half and introducing a canceling symmetry between the two halves [Spence 1991]. The first half-solenoid rotates the beam about the longitudinal axis by $\psi_s/2$ while the spin rotates by ψ_s. If this is followed by a transfer matrix which is $+I$ in the x-plane and $-I$ in the y-plane, the beam is reflected about the y-axis where another half-solenoid of equal strength rotates the beam to its flat state again and a net spin precession of $2\psi_s$ is accomplished. If $k \equiv \psi_s/2L_s = B_z/2(B_0\rho)$, the transfer matrix of the solenoid [Brown 1980] is

$$R_s = \begin{pmatrix} C^2 & SC/k & SC & S^2/k \\ -kSC & C^2 & -kS^2 & SC \\ SC & -S^2/k & C^2 & SC/k \\ kS^2 & -SC & -kSC & C^2 \end{pmatrix} \quad . \tag{5.5}$$

Inserting the reflector beam line between the two solenoids produces a system transfer matrix of

$$R_s \begin{pmatrix} 1 & 0 & 0 & 0 \\ 0 & 1 & 0 & 0 \\ 0 & 0 & -1 & 0 \\ 0 & 0 & 0 & -1 \end{pmatrix} R_s = \begin{pmatrix} \cos\psi_s & k^{-1}\sin\psi_s & 0 & 0 \\ k\sin\psi_s & \cos\psi_s & 0 & 0 \\ 0 & 0 & \cos\psi_s & k^{-1}\sin\psi_s \\ 0 & 0 & k\sin\psi_s & \cos\psi_s \end{pmatrix} \quad . \tag{5.6}$$

As long as the solenoids have equal strength ($\pm$ ~1% in this case), all $x-y$ coupling is canceled independent of solenoid settings; the solenoid pairs will be powered in series to insure comparable strengths. Finally, the focusing dependence can be compensated with matching quadrupoles.

Location of the Rotator

Solenoid rotator systems are limited to low-energy applications due to the necessary scaling of solenoid strength with energy. For the NLC, this may seem like a major disadvantage since the second bunch compressor at 10 GeV

includes a 180° arc and the beam delivery section (Collimation–Final Focus) includes a 10-mr arc at 500 GeV to achieve the 20-mr crossing angle. These bends will rotate a non-vertically oriented spin vector many times, potentially depolarizing the beam due to the incoming energy spread. However, a calculation of this depolarization shows it to be small. If the bunch compressor arc at 10 GeV bends the beam by π, the spin will be rotated by $\psi_s = \alpha\gamma_0(1+\delta)\pi$ (11.4 turns) while the beam delivery arc at 500 GeV will rotate the spin vector by 1.8 turns. The change in the spin magnitude will be $P(\delta)/P_0 = \cos(\alpha\gamma_0\delta\pi)$ and the mean polarization over a beam with a Gaussian energy spread σ_δ is

$$\bar{P}/P_0 = \frac{1}{\sqrt{2\pi}}\sigma_\delta \int_{-\infty}^{\infty} e^{-\delta^2/2\sigma_\delta^2}\cos(\alpha\gamma_0\delta\pi)\,d\delta = e^{-(\alpha\gamma_0\pi\sigma_\delta)^2/2} \quad . \tag{5.7}$$

For an energy spread of $\sigma_\delta = 0.25\%$ in the 10-GeV 180° arc, the relative depolarization is 1.6%; it is roughly five times smaller through the beam delivery system. Therefore, the solenoid-based rotator system can be placed at 2 GeV immediately after damping ring extraction with little spin diffusion. Note that the net spin rotation in the low-energy compressor wiggler and the high-energy compressor chicane are zero since there is no net bending and thus these sections cause no depolarization.

Rotator Flexibility

A fully flexible rotator can be made by placing a short horizontal bending section between two split-solenoid segments as previously described. If the four solenoids are each capable of providing a maximum ±45° of spin rotation around the longitudinal axis and the bend section provides 90° around the vertical axis, the system will provide arbitrary control of the IP spin orientation as long as the spin sign is reversible by some means prior to damping. The net spin rotation through the system is symbolized in Eq. 5.8.

$$\Omega_{\rm tot} = \Omega_{sol/34}\Omega_{bend}\Omega_{sol/12} = \begin{pmatrix} c_3 & -s_3 & 0 \\ s_3 & c_3 & 0 \\ 0 & 0 & 1 \end{pmatrix}\begin{pmatrix} c_2 & 0 & s_2 \\ 0 & 1 & 0 \\ -s_2 & 0 & c_2 \end{pmatrix}\begin{pmatrix} c_1 & -s_1 & 0 \\ s_1 & c_1 & 0 \\ 0 & 0 & 1 \end{pmatrix} \tag{5.8}$$

Here $c_i \equiv \cos(\psi_i)$, $s_i \equiv \sin(\psi_i)$, where ψ_i is the spin rotation of the ith section and $i = 1,2,3$ indicates the first solenoid pair, the bend section, and the second solenoid pair respectively. Since the input spin vector from damping ring extraction will be vertical, the spin vector after the full system is

$$\bar{s} = \Omega_{\rm tot}\begin{pmatrix} 0 \\ \pm 1 \\ 0 \end{pmatrix} = \begin{pmatrix} \mp\big(\sin(\psi_3)\cos(\psi_1) + \cos(\psi_2)\cos(\psi_3)\sin(\psi_1)\big) \\ \pm\big(\cos(\psi_3)\cos(\psi_1) - \cos(\psi_2)\sin(\psi_3)\sin(\psi_1)\big) \\ \pm\sin(\psi_2)\sin(\psi_1) \end{pmatrix} \quad . \tag{5.9}$$

If the solenoid fields are reversible, then any arbitrary spin orientation is achievable at the nominal beam energy of 2 GeV where $\sin(\psi_2) = 1$; there is a slight loss in the tunable orientation when the damping ring energy is raised or lowered but this is not expected to be significant.

Rotator Beam Line Optics

The reflector beam line (between solenoids) is built with four FODO cells each with 90° betatron phase advance in x and 45° in y. Three cells of 120°, 60° are possible; however, the chromaticity of the 120° cells is larger than desirable. The short bend section (mini-arc) is a simple missing magnet scheme containing six horizontal bend magnets and four 90° x and y FODO cells. The net horizontal bend angle at 2 GeV is $\pi/2\alpha\gamma = 19.83°$. The peak horizontal dispersion is 260 mm and the total R_{56} is 40 mm.

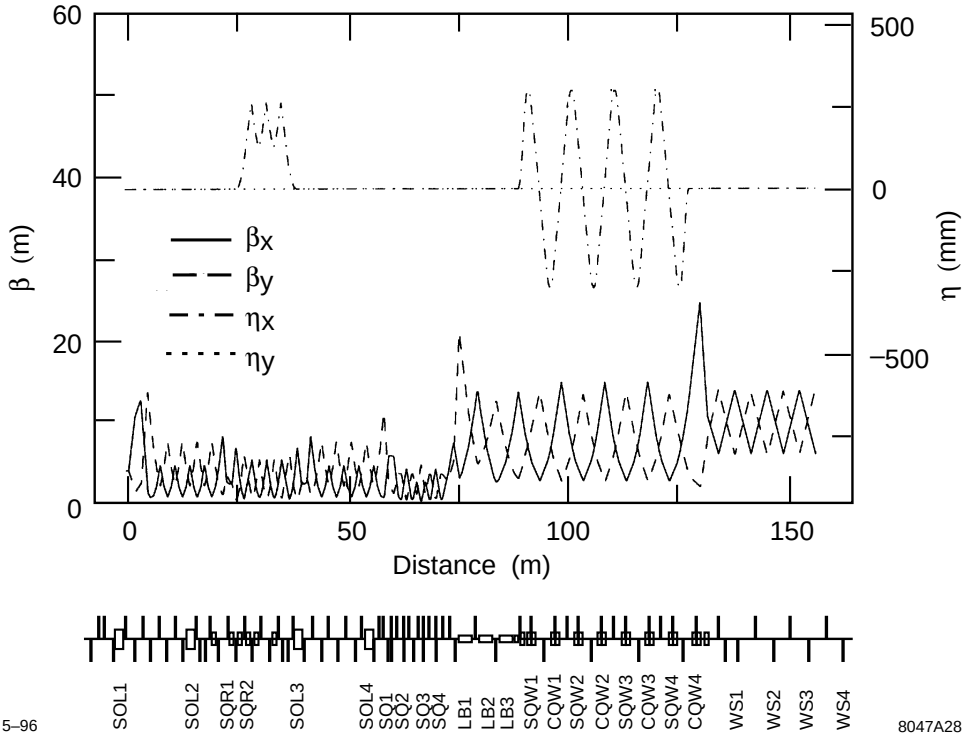

Figure 5-2. *Dispersion and beta functions for the entire low-energy bunch compressor and spin rotator system. Tuning elements and major component locations are indicated. Notation is explained in Section 5.5.*

The solenoids are 1.50 m in length with a maximum field strength of ± 38.5 kGauss; this will rotate the spin by 45° at a beam energy of 2.2 GeV. There is also a four-quadrupole beta matching section between the first solenoid pair segment and the mini-arc, and another matching section between the mini-arc and the second solenoid pair segment. These matching sections are used to maintain the periodic beta functions in the mini-arc through all possible solenoid settings. This is necessary since the solenoids radially focus the beam. The reflector sections provide coupling cancelation while the matching sections provide constant beta functions at the output of the entire system. Figure 5-2 shows the lattice functions for the combined spin rotator and first bunch compressor while Figure 5-3 shows the beta functions of the spin rotator system with (a) solenoids off and (b) solenoids on. With the solenoids at full strength, the x and y beta functions between them are strongly coupled creating very large vertical beta functions due to the locally rolled beam. The dispersion functions are shown in Figure 5-3c.

Chromaticity of the Rotator System

It is important to cancel the large solenoid coupling over a range of particle energies which is comparable to the beam energy spread. The reflector beam line transfer matrix will break down at some level for off-energy particles resulting in energy dependent-coupling. By locating the solenoid rotator system immediately after damping ring extraction and before the first bunch compressor rf section, the energy spread in the solenoids is small ($\sim$0.1% rms). This bandpass is easily achieved in the worst case (all four solenoids at maximum strength) by using FODO cells with $\leq$90° phase advance. Figure 5-4 shows the mono-energetic system bandpass with all four solenoids at full strength, ψ_s(pair) = $\pi/2$. Figure 5-5 shows the emittance as the Gaussian rms energy spread is increased. The vertical emittance increase at 0.1%-rms Gaussian energy spread is $<$0.5%.

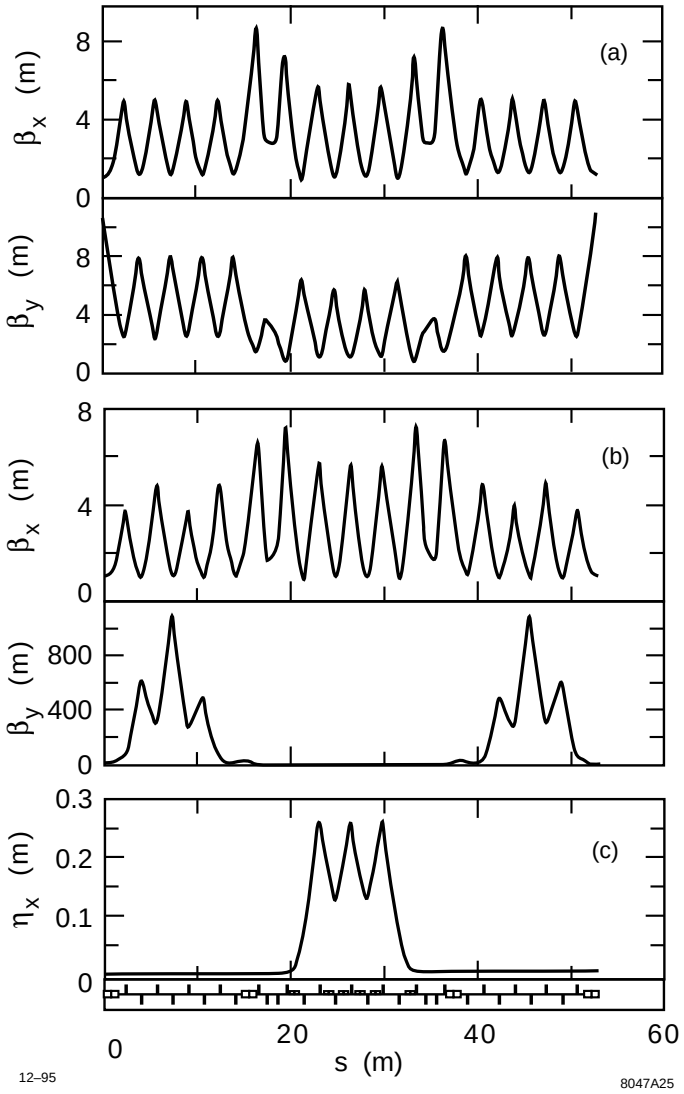

Figure 5-3. *(a) Horizontal and vertical beta functions for spin rotator system with all four solenoids switched off. (b) Beta functions with all solenoids at maximum field, ϕ_s(pair) = $\pi/2$. (c) Horizontal dispersion function for spin rotator system (same for solenoids off or on); the vertical dispersion is zero.*

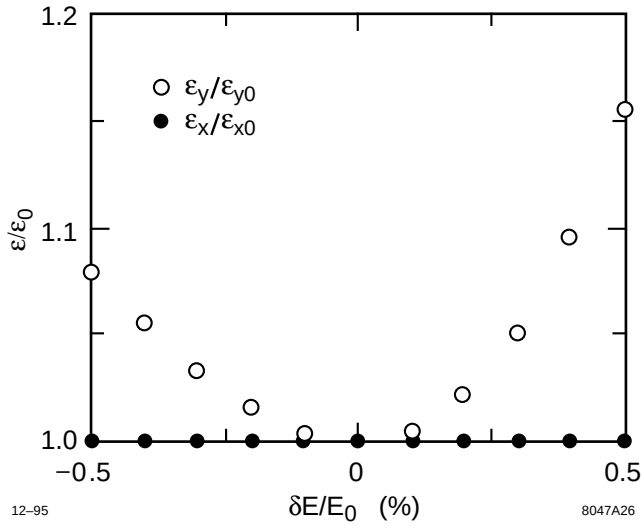

Figure 5-4. *Energy bandpass of the complete solenoid-based rotator system for a mono-energetic beam. The emittance values used are* $\gamma\epsilon_{x_0} = 2.3 \times 10^{-6}$ *m,* $\gamma\epsilon_{y_0} = 2.3 \times 10^{-8}$ *m.*

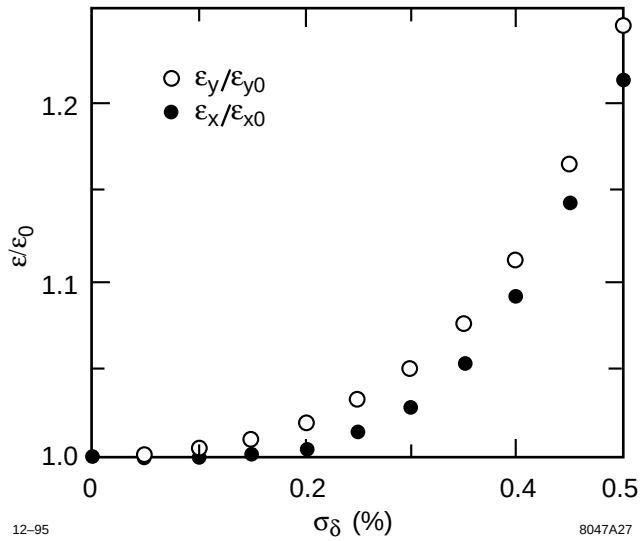

Figure 5-5. *Gaussian rms energy spread dependence of relative chromatic emittance growth.*

Longitudinal Phase Space and Synchrotron Radiation

The rotator system has very little impact on the performance of the first bunch compressor. The longitudinal transfer matrix of the first bunch compressor, not including the spin rotator, is (see Section 5.3.4)

$$\mathbf{R}_{\rm bc1} = \begin{pmatrix} 1+fR_{56} & R_{56} \\ f & 1 \end{pmatrix} \quad . \tag{5.10}$$

To minimize the final bunch length after compression, the rf parameter, f, is chosen so that $1 + fR_{56} = 0$. In this case, adding the spin rotator system with $\alpha \equiv R_{56}$(rot) changes only the R_{66} element of the the total transfer matrix.

$$\mathbf{R}_{\rm bc1}\mathbf{R}_{\rm rot} = \begin{pmatrix} 0 & R_{56} \\ f & 1 \end{pmatrix} \begin{pmatrix} 1 & \alpha \\ 0 & 1 \end{pmatrix} = \begin{pmatrix} 0 & R_{56} \\ f & 1+\alpha f \end{pmatrix} \tag{5.11}$$

The bunch length after the first compression in unchanged by the rotator and the energy spread after compression is insignificantly smaller ($f = 2\,\mathrm{m}^{-1}, \alpha = -0.04\,\mathrm{m}$).

$$\sigma_{zf} = \sigma_{\delta i} R_{56} \quad , \quad \sigma_{\delta f} = \sqrt{\sigma_{zi}^2 f^2 + \sigma_{\delta i}^2 (1+\alpha f)^2} \tag{5.12}$$

Feedback, Tuning, and Diagnostics Sections

The tightest tolerances on this system are in the construction of the reflector beam line. Without any tuning correction, one of the eight quadrupoles in the reflector would have to be built with a gradient which meets the absolute specification to an accuracy of ∼0.2% to limit the vertical emittance increase to 2%; most other quadrupoles are significantly looser in this tolerance. In any case, a small tunable coupling correction section is already needed to minimize damping ring extraction coupling and this same correction section can be used to cancel any residual coupling due to reflector imperfections.

The tuning of the spin rotator optics, *i.e.,* the betatron match and coupling, will be done with the bunch compressor rf off and use an emittance diagnostic section located at the end of the first bunch compressor–this is described in Section 5.3.4; this procedure is similar to that used in the SLC bunch compressors. The tunability of this system has been studied in some detail using the *Final Focus Flight Simulator* program [Woodley 1994]. To facilitate the tuning, four skew quadrupoles are placed at the end of the rotator system in locations with appropriate phase advances so they are, at least initially, orthonormal to each other [Emma 1995]. In addition, two more skew quadrupoles are placed in the 20° arc to correct any residual vertical dispersion. This system can then be easily compensated for random quadrupole gradient errors of 1% rms and is discussed further in Section 5.5.

Because of the small incoming energy spread, the alignment tolerances are relatively loose, $\sim 50\ \mu$m. Regardless, the alignment of the solenoids and quadrupoles will be adjusted using remote magnet movers similar to those developed for the FFTB. All of the quadrupoles have internally-mounted BPMs and independent power supplies to facilitate the alignment; the tolerances are discussed further in Section 5.6.

Finally, as described earlier, there will be a fast-feedback system in the ring extraction line to control the extraction positions and angles from the damping rings. Because the alignment and vibration tolerances are relatively loose, no other feedback systems are expected in this region.

Energy	2 GeV
σ_z	5 mm $\rightarrow$ 500 μm
σ_ϵ	0.1% $\rightarrow$ 1.0%
V_{rf}	139 MV
f_{rf}	1.4 GHz
L_{rf}	10 m
$\phi_{\rm rf}$	$-101°$
R_{56}	0.5 m
$\Delta\epsilon_{SR}/\epsilon$	$\sim$1.3%
Bend Hor. Aperture	4 cm
Quad. Aperture	1 cm
Length	100 m

Table 5-2. *Parameters for 2-GeV compressor.*

5.3.4 Low-Energy Compressor

The low-energy bunch compressors follow the spin rotators. Assuming an rms energy spread of $\sigma_\delta = 1 \times 10^{-3}$, they compress the damping ring beam to a bunch length of $500\ \mu$m. The final bunch length is roughly independent of the incoming bunch length and the system has been designed to accept an initial bunch length of 5 mm; this is 25% larger than expected from the damping ring. The bunch compressors consist of a 139-MV L-band (1.4 GHz) rf section followed by a long period wiggler which generates the R_{56} needed for the bunch compression; parameters are listed in Table 5-2.

The compressors are designed to rotate the longitudinal phase space by roughly $\pi/2$. This prevents synchronous phase errors, originating due to the transient beam loading in the damping rings, from becoming phase errors, and thereby extraction energy errors, in the linacs. Of course, the phase tolerance is then reflected on the phase stability of the compressor rf system—one reason for choosing the L-band rf frequency is that it is much less sensitive to the multibunch loading which manifests itself as a phase error.

A "$\pi/2$" compressor can be constructed from an rf section introducing a $\delta - z$ correlation and a bending system where the path length is energy-dependent. The linear equations determining the parameters are simple. The transfer matrix is:

$$\mathbf{R} = \begin{pmatrix} 1 + fR_{56} & R_{56} \\ f & 1 \end{pmatrix} \quad , \tag{5.13}$$

where

$$f \equiv \frac{d\delta}{dz} = -\frac{Vk\sin\psi}{E_o + V\cos\psi} \quad . \tag{5.14}$$

Here, R_{56} is the R_{56} of the bending system, V is the rf voltage, k is the rf wave number, and ψ is the rf phase where $0°$ corresponds to running on the rf crest. Finally, the compressed phase, energy, bunch length, etc., are given by:

$$z_f = z_i(1 + fR_{56}) + \delta_i R_{56} \tag{5.15}$$

$$\delta_f = z_i f + \delta_i \tag{5.16}$$

$$\sigma_{zf}^2 = \sigma_{zi}(1 + fR_{56})^2 + 2\langle\delta_i z_i\rangle R_{56}(1 + fR_{56}) + \sigma_{\delta i}^2 R_{56}^2 \tag{5.17}$$

$$\sigma_{\delta f}^2 = \sigma_{zi}^2 f^2 + 2\langle\delta_i z_i\rangle f + \sigma_{\delta i}^2 \tag{5.18}$$

$$\langle\delta_f z_f\rangle = \sigma_{zi}^2 f(1 + fR_{56}) + \langle\delta_i z_i\rangle(1 + 2fR_{56}) + \sigma_{\delta i}^2 R_{56} \tag{5.19}$$

For full compression, the R_{56} is determined by the initial energy spread and the desired bunch length. The rf parameters are chosen so that $f = -1/R_{56}$. In such a design, the only free parameters are the rf frequency and the rf phase—all other parameters are determined by the input beam. Finally, note that such a compressor does not really rotate the longitudinal phase space by $\pi/2$, but the final phase is independent of the initial phase as desired.

Wiggler

The bending system used to generate the R_{56} for the low-energy compressor is constructed as a very long period wiggler. Quadrupoles are placed between the dipoles in locations where the dispersion passes through zero. In this manner, they can constrain the beta functions but they will not generate any second-order dispersion and do not need large apertures. This eliminates the need for strong sextupole magnets which would have tight vertical alignment tolerances due to the coupling they introduce—sextupole correctors and other multipole fields will still be required for tuning purposes. Four wiggler cells are used with a 90° phase advance per cell to reduce the sensitivity to systematic errors in the bending magnets. The optical functions for the entire low-energy compressor, including spin rotator, rf section, and diagnostics section are plotted in Figure 5-2.

The bending magnets and quadrupoles for the low-energy compressor are straightforward. The required apertures are listed in Table 5-2. The main bending magnets are 1.2 m in length with a magnetic field of 14 kGauss; they will be powered as a string by a single power supply to reduce the regulation tolerance on the supply. The quadrupoles are 15 cm in length and have pole-tip fields that are less than 7 kGauss. They will be powered by independent power supplies and mounted on remote magnet movers to facilitate the beam based tuning.

RF Section

The rf section consists of two 5-m L-band rf structures that provide a total rf voltage of 139 MV and operate at a phase of $-101°$ which is slightly past the nominal $-90°$; this is to compensate the T_{566} generated in the wiggler. These structures are located in FODO cells just prior to the beginning of the wiggler. The multibunch beam loading compensation is accomplished using the ΔT method (early injection) and is discussed in Chapter 6. To facilitate the alignment, both structures will be instrumented with rf BPMs and will be mounted on remote movers.

Feedback, Tuning, and Diagnostic Sections

Because of the small beam emittances, the alignment and field tolerances in the compressor would be tight. Fortunately, it is straightforward to use simple tuning techniques to ease the tolerances substantially. The quadrupoles will be powered with independent power supplies and will be mounted on remote movers to facilitate the alignment and the optical tuning will be performed using an emittance diagnostic section consisting of four laser wires located after the compressor wiggler. This is followed by a beam dump that will allow full operation of the damping rings and compressor systems for tuning and commissioning purposes.

Four weak skew quadrupoles and four weak normal quadrupoles will be placed in the dispersive regions of the wiggler to facilitate the tuning of the horizontal and vertical dispersion. In addition, four skew sextupoles will be added to control the vertical second order dispersion. All of the tuning elements and procedures are described in Section 5.5.

The rf voltage and phase of the L-band cavity can be calibrated by varying the rf phase and measuring the beam centroid offsets in the wiggler section. It is more difficult to tune the beam loading compensation in the rf structures. This will be done using a beam phase monitor located at the end of the bunch compressor with a phase resolution of

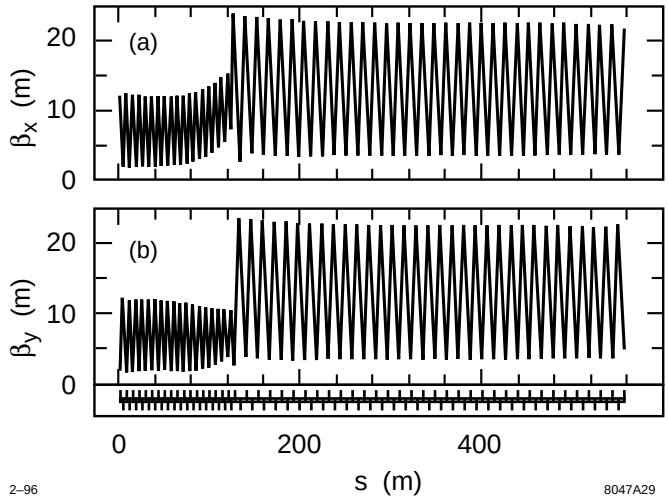

Figure 5-6. *Optical functions in S-band prelinac.*

0.1° S-band. Finally, there will be a phase feedback system that will measure the bunch train centroid through the wiggler and adjust the damping ring synchronous phase; this is discussed in Chapter 4.

5.3.5 Prelinac

Optical Design

The optical design of the prelinac consists of simple FODO cells with an initial quadrupole spacing of 3.1 m to accommodate the 3-m S-band structures. As the beam energy is increased, the quadrupole spacing is increased to a 6-m spacing, accommodating two accelerator structures between quadrupoles. The matching across this transition has been tuned to have a bandwidth in excess of 20%. Finally, note that the horizontal and vertical phase advances are separated by roughly 5%. This reduces the sensitivity to systematic skew quadrupole fields and the nonlinear betatron coupling due to the beam space charge field and trapped ions [Raubenheimer 1992]. The lattice functions are plotted in Figure 5-6.

The quadrupoles are 10 cm in length and have a 1-cm radius with pole-tip fields less than 7.6 kGauss. As is standard practice in the NLC, all of the linac quadrupoles will have internal BPMs and will be mounted on remote magnet movers. In addition, all of the quadrupoles are powered by independent power supplies. This will allow the electrical centers of the BPMs to be accurately determined with respect to the magnetic centers of the quadrupoles and then the quadrupoles can be aligned by adjusting the movers.

RF System

The S-band prelinac consists of 3-m DDS S-band accelerating structures—the structures, klystrons, and rf pulse compressors are described in greater detail in Chapter 6. The linac consists of 33 rf modules with four accelerator structures per module. Each module is powered with two 5045 klystrons and a SLED pulse compressor to produce a net acceleration of 254 MeV. Thus the linac can provide 8.4 GeV of acceleration and would normally operate with one

rf module in standby. The multibunch beam loading is compensated using the ΔT method (early injection) so that the bunch-to-bunch energy deviations are corrected locally in each structure; this minimizes the emittance growth due to dispersive and chromatic effects. The expected bunch-to-bunch energy variation is less than 10^{-4}; this is discussed in Chapter 6.

Finally, all of the accelerator structures will have rf BPMs and will also be mounted on girders that can be remotely aligned; there is one structure support girder between quadrupoles and thus at the beginning of the prelinac there is only one structure per girder while at the end of the linac there are two structures per girder. This will allow the structures to be aligned to the beam trajectory. The alignment techniques are described in Section 5.5.

Feedback, Tuning, and Diagnostic Sections

As noted earlier, there is a diagnostic section, consisting of four laser wire scanners, after the low-energy bunch compressor at the beginning of the prelinac. This is followed by a pulsed dump which can absorb a full bunch train at the nominal repetition rate so that the damping rings and first bunch compressors can be tuned before the beams are sent through the prelinacs.

A second diagnostic section, again consisting of four laser wire scanners, is located at the end of the prelinac. To save space, this section is integrated into the linac lattice. It is followed by another pulsed beam dump to facilitate the tuning of the prelinac. As described, the transverse alignment of the quadrupoles and accelerator will be performed using remote magnet movers; details are described in Section 5.5.

The rf phases and the beam loading compensation will be tuned using the spectrometer in the beam dump or using the 180° arc as a spectrometer. The BPMs in the arc have a resolution of 1 μm and will be able to resolve relative energy variations of roughly 10^{-5}; this is more than sufficient to optimize the klystron phases and the beam loading compensation.

Finally, one fast-feedback system will be used to control the transverse position and angle of the bunch train as it is injected into the prelinac and another will be located at the transition region where the quadrupole spacing is increased from 3 to 6 m. In addition, an energy feedback will be used to stabilize the beam energy; this will adjust the phases of the two klystrons feeding one of the rf modules to vary the beam voltage.

5.3.6 High-Energy Compressor

The high-energy bunch compressors follow the prelinacs. Assuming an rms bunch length of $\sigma_z = 500\,\mu$m, they compress the beam to a bunch length between 100 and $150\,\mu$m depending on the NLC parameters. The bunch compressors consist of a 180° arc which is followed by a 4-GeV S-band (2.8 GHz) rf section and a chicane. Parameters of the high-energy bunch compressors are listed in Table 5-3 for four different NLC scenarios.

As described, the second compressor is designed to rotate the longitudinal phase space by 2π; it is a telescope in longitudinal phase space. This requires two rf sections and two bending regions. We can use the prelinac as the first rf region. Then, a 180° arc will be used for the first bending region, followed by an rf section and then a magnetic chicane as the second bending region. The linear equations that determine the compressor are:

$$\mathbf{R} = \begin{pmatrix} 1 + f_2 R_{56\,2} + f_1(f_2 R_{56\,1} R_{56\,2} + R_{56\,1} + R_{56\,2}) & R_{56\,1} + R_{56\,2} + f_2 R_{56\,1} R_{56\,2} \\ f_1 + f_2 + f_1 f_2 R_{56\,1} & --- \end{pmatrix}, \tag{5.20}$$

	NLC-I a	NLC-I c	NLC-II a	NLC-II c
Energy	10 GeV			
Initial σ_z	500 μm			
Final σ_z	100 μm	150 μm	125 μm	150 μm
Initial σ_ϵ	0.25 %			
Final σ_ϵ	1.5 %	1.2 %	1.3 %	1.4 %
180° arc R_{56}	0.211	0.147	0.184	0.162
Arc Length	330 m			
$\Delta\epsilon_{SR}/\epsilon$ (arc)	2.2%	1.5%	2.0%	1.6 %
$V_{\rm rf}$ (GV)	3.85	3.50	3.73	3.61
$f_{\rm rf}$	2.8 GHz			
$L_{\rm rf}$	250 m			
$V_{{\rm rf}\ c}$ (MV)	274	226	256	240
$f_{{\rm rf}\ c}$	11.4 GHz			
$L_{{\rm rf}\ c}$	7.6 m			
Chicane R_{56}	36 mm			
Chicane Length	100 m			
$\Delta\epsilon_{\rm SR}/\epsilon$ (chicane)	$\sim 0.05\%$			
Bend Hor. Aperture	10 cm			

Table 5-3. *Parameters for 10-GeV compressor.*

where $R_{56\,1}$ and $R_{56\,2}$ are the R_{56}s of the first and second bending regions and f_1 and f_2 are the rf parameters for the first and second rf regions. Finally, the (2,2) matrix element can be found from the other (the determinant equals 1) but it is not relevant for our study.

To make the final phase independent of the incoming energy and only sensitive to the incoming phase, we require that the (1,2) matrix element equal zero. In addition, to compress the bunch by a factor m, we require that the first matrix element be equal to $\pm 1/$ m. Finally, to perform a full $n\pi$ rotation, we require that the (2,1) element also be zero, but this is not actually very important for us since the incoming phase errors should be small. Thus, no restriction needs to be placed on the rf of the prelinac and the two constraints on the compressor design are:

$$1 + f_2 R_{56\,2} = \pm 1/m \qquad\qquad R_{56\,1} = \mp m R_{56\,2} \tag{5.21}$$

where the upper sign corresponds to a 2π rotation and the lower signs are for a π rotation of the phase space.

Because the NLC collider geometry suggests using a 180° arc and a chicane which have opposite values of R_{56}, we have designed the compressor to perform a 2π rotation. Now, given a value of the R_{56} in the chicane and a chosen rf frequency (S-band), the R_{56} of the arc and the parameters of the rf section between the arc and the chicane are determined. To reduce nonlinearities of the longitudinal phase space, the R_{56} of the chicane should be as small as possible. However, a smaller R_{56} increases the required rf voltage, so a compromise had to be found. According to longitudinal single-bunch simulations, an R_{56} of 100 mm is too large and impairs the performance of the compressor. In the present design, therefore, the R_{56} of the chicane is chosen as 36 mm, which implies a 200-m-long S-band rf section.

Parameter	Symbol	Unit	$\psi_x = 90°$	$\psi_x = 108°$	$\psi_x = 135°$
Momentum compaction	R_{56}	m	-0.286	-0.208	-0.150
Synch. rad. emit. growth	$\Delta\epsilon_{\rm SR}/\epsilon_0$	%	3.7	2.4	1.6
Max. hor. beta function	$\beta_x^{\rm max}$	m	7.27	7.67	10.35
Max. hor. dispersion function	$\eta_x^{\rm max}$	m	0.133	0.102	0.078
F-quad pole-tip magnetic field	B_{QF}	kGauss	$+7.15$	$+8.08$	$+9.26$
D-quad pole-tip magnetic field	B_{QD}	kGauss	-7.15	-7.32	-7.50
F-sext. pole-tip magnetic field	B_{SF}	kGauss	$+1.18$	$+1.74$	$+2.63$
D-quad pole-tip magnetic field	B_{QD}	kGauss	-2.06	-2.98	-4.43
# FODO cells	$N_{\rm cell}$	—	68		
Energy	E	GeV	10		
Total arc length	$L_{\rm tot}$	m	295		
Total bend angle	θ	°	180		
Mag. length of quadrupoles	L_Q	m	0.32		
Mag. length of dipoles	L_B	m	1.25		
Mag. length of sextupoles	L_S	m	0.10		
Drift between every magnet	$L_{\rm BPM}$	m	0.3		
Vert. betatron phase adv. per cell	ψ_y	°	90		
Quadrupole magnet pole radius	r_Q	mm	10		
Sextupole magnet pole radius	r_S	mm	10		
Bend angle of dipole	θ_B	°	1.304		
Bend radius of dipole	ρ	m	54.9		
Spin advance per cell	$\Phi_{\rm Spin}$	°	59.2		

Table 5-4. *Parameters for 180° arc of high-energy compressor for several momentum compaction factors adjusted by varying the x-betatron phase advance per cell, ψ_x.*

Arc

The bending system used to generate the R_{56} for the 180° arc is constructed from a series of FODO cells. Although one could reduce the emittance growth through this section using combined-function bending magnets, we have chosen separated-function magnets so that one can use beam-based alignment techniques to align the quadrupole magnets.

We have studied several versions of the arc, with different numbers of cells. In all cases, the R_{56} is easily adjusted with the horizontal phase advance and the choice of the number of cells depends upon the tuning range desired. The present arc design consists of 68 FODO cells, and has an average radius of about 100 m. Variation of the horizontal phase advance per cell from 90° to 135° changes the R_{56} from 29 cm to 15 cm, which results in an increase of the final bunch length from 100 μm to 150 μm. This variability covers the entire NLC operating plane. While the horizontal phase advance is varied, the vertical phase advance per cell is held constant at 90°. Figure 5-7 illustrates the tuning range of the R_{56} in the arc and the corresponding emittance growth due to synchrotron radiation. In addition, the beta functions and dispersion functions are plotted in Figures 5-8 and 5-9. Finally, the arc parameters are summarized in Table 5-4.

The arcs are constructed using bending magnets that are 1.25 m in length and have a maximum field of 6 kGauss and quadrupole magnets that are 32-cm long and have a 1-cm radius with pole-tip fields of 8 kGauss. To relax the stability and voltage requirements on the bending magnet power supplies, 18 bends are powered as a string by a single power supply. As stated, all of the quadrupoles have independent power supplies to facilitate the beam-based alignment.

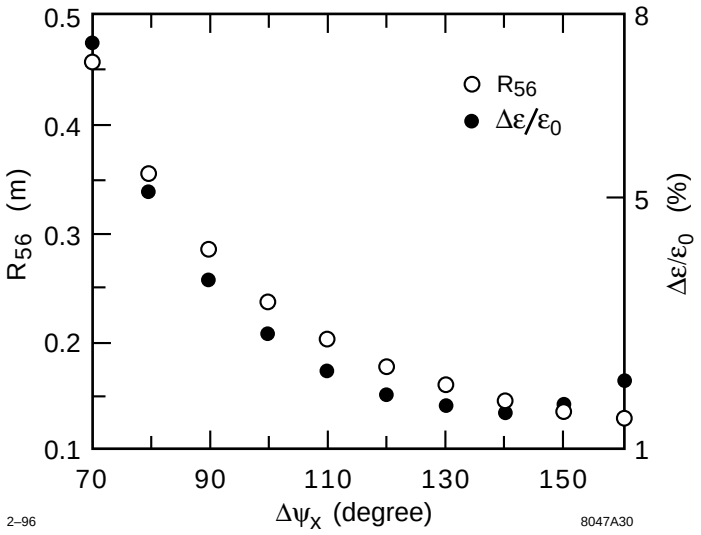

Figure 5-7. *R_{56} (solid) and $\Delta\epsilon_x$ (dashes) for 68-cell arc.*

Sextupole compensation is also included in the optical design to desensitize the arc to the generation of dispersion due to incoming betatron oscillations. This also desensitizes the arc to the generation of second order dispersion due to a dispersion oscillation through the entire arc. Without sextupole compensation a vertical betatron oscillation (jitter) which propagates through the entire arc will generate vertical dispersion due to the chromaticity of the quadrupoles. For an initial oscillation amplitude of $\eta_\sigma = y_0/\sqrt{\beta_y \varepsilon_{y0}}$ in the first QD ($y_0' = 0$) which oscillates through an arc with $N(\gg 1)$ FODO cells of phase advance per cell μ and rms energy spread σ_δ, the vertical emittance dilution due to dispersion is approximately (thin lens QDs only)

$$\frac{\Delta\varepsilon}{\varepsilon_0} \approx \frac{1}{2}\left(n_\sigma N \sigma_\delta \frac{1+\sin\mu/2}{\cos\mu/2}\right)^2 \quad . \tag{5.22}$$

For the high-energy bunch compressor (BC2) arc parameters without sextupoles, an initial vertical oscillation of $n_\sigma = 1$ ($y_0 = 3.3\,\mu$m) would induce a 10% emittance dilution due to vertical dispersion. Likewise, a small vertical dispersion error of 1 mm (at QDs) through the entire arc would generate second-order dispersion which dilutes the emittance by 10%. The inclusion of sextupoles opens these oscillation tolerances by more than a factor of 10 and actually allows full recovery of the emittance using the simple linear tuning schemes discussed in Section 5.5.3, even for extreme vertical emittance dilution cases of $\Delta\varepsilon_y/\varepsilon_{y0} \sim 30$. The sextupoles are 10-cm long with 1-cm pole radius and 1.7 and -3.0 kGauss pole-tip fields for the `focusing' (SF) and `defocusing' (SD) sextupoles, respectively. Their alignment tolerances are similar to the quadrupole alignment tolerances of roughly $60 \sim 100\,\mu$m and are discussed in Section 5.5.3.

Figure 5-10 is a plot of the emittance dilution, without synchrotron radiation effects, at the end of the 68-cell arc as a function of the incoming energy spread for a horizontal phase advance of 108°. For the nominal operation parameters, the emittance growth is less than 0.5%.

RF Section

The high-energy bunch compressor rf sections consist of roughly 4 GeV of S-band linac. The linacs are similar to the S-band prelinacs, consisting of 3-m DDS S-band accelerator structures. They differ from the prelinacs in

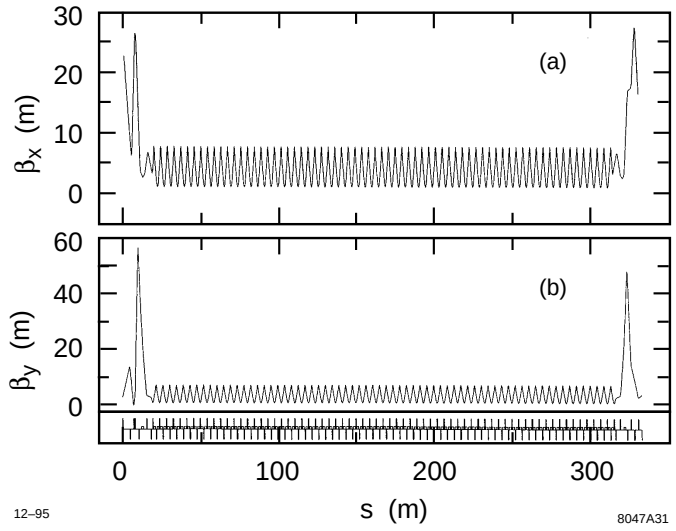

Figure 5-8. *Beta functions for 68-cell arc.*

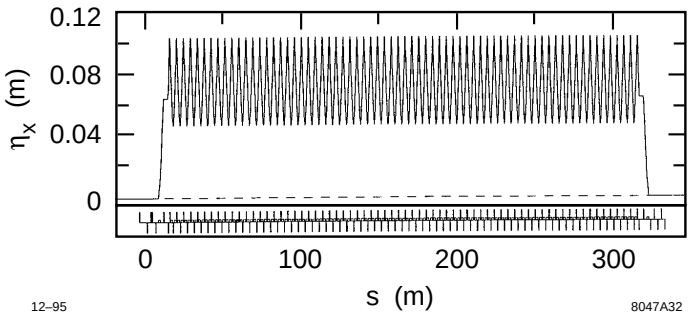

Figure 5-9. *Dispersion function for 68-cell arc.*

that the multibunch beam loading is compensated using a combination of the ΔT method (early injection) and the ΔF method; this is necessary to attain the required compensation. The linacs consist of 16 rf modules with a net acceleration of 253 MeV per module. Thus, they can provide 4 GeV of acceleration and would normally operate with at least one rf module in standby; see the parameters in Table 5-3. Each module has five accelerator structures, four tuned to the nominal frequency and one structure that is either 1.1 MHz above the nominal 2.856 GHz or 1.1 MHz below 2.856 GHz; the sign of the frequency compensation alternates between modules. The four normal structures in each module are powered with two 5045 klystrons and a SLED pulse compressor while the off-frequency structure is powered with a single 42-MW klystron. The structures, klystrons, rf pulse compressors, and beam loading compensation are described in greater detail in Chapter 6.

Because the bunch length is long in these rf sections, the transverse wakefields are significant. Furthermore, because the chicane will rotate the longitudinal phase space, the transverse emittance dilutions will not be correctable after the beam passes the chicane. To reduce the emittance dilution, this rf section has strong focusing with a 3.1-m quadrupole spacing. To attain the required fields, the quadrupoles are 15 cm in length with a 1-cm aperture and maximum pole-tip fields of 7 kGauss.

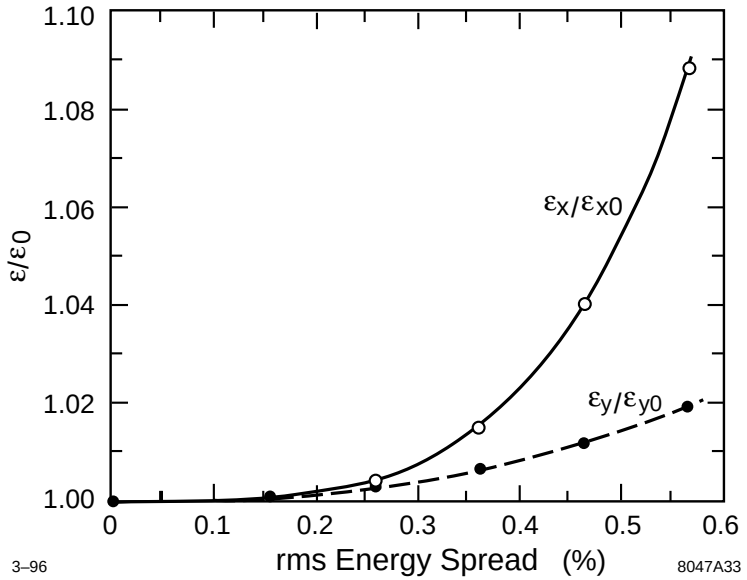

Figure 5-10. *Chromatic emittance growth for nominal operation, ($R_{56} = 210$ cm).*

Finally, the high-energy compressor also needs a higher frequency rf to compensate the T_{566} from the chicane. The present design requires roughly 275 MV of X-band rf provided in three 1.8-m structures.

Chicane

The chicane is constructed from sixteen 2.5-m bending magnets having a 1.1-kGauss field; the beta functions and the dispersion function are plotted in Figures 5-11 and 5-12. The lengths and spacing are chosen so as to achieve the R_{56} of 3.6 cm in a reasonable length, without generating substantial emittance dilution due to synchrotron radiation; all of these are subjective constraints and the parameters might be optimized in another manner.

One potential issue is the peak value of the dispersion which is roughly 65 cm. This means that the horizontal good field aperture of the bending magnets must be large ($\sim$ 10 cm full width) to provide an aperture in excess of ± 5 sigma and without tuning correction, the alignment and field tolerances will be severe. The field tolerances can be attained by using large aperture magnets and careful construction techniques and, fortunately, the tuning of the errors is straightforward as described in Section 5.5.

Feedback, Tuning, and Diagnostic Sections

A diagnostic section consisting of four laser wires is located at the end of the chicane so that the chromatic properties of the chicane can be tuned properly for injection into the main X-band linacs. Presently, it is thought that the 180° arc and the rf section can be tuned by turning the compressor rf off to minimize the beam energy spread and using the diagnostic section at the end of the chicane. If necessary, an additional diagnostic section can be integrated into the end of the high-energy compressor rf section before the chicane. Finally, there are pulsed beam dumps just before the beginning of the main linacs that allow the whole injector complex to be tuned before accelerating the beams to high energy; the tuning elements and procedures are described in Section 5.5.3.

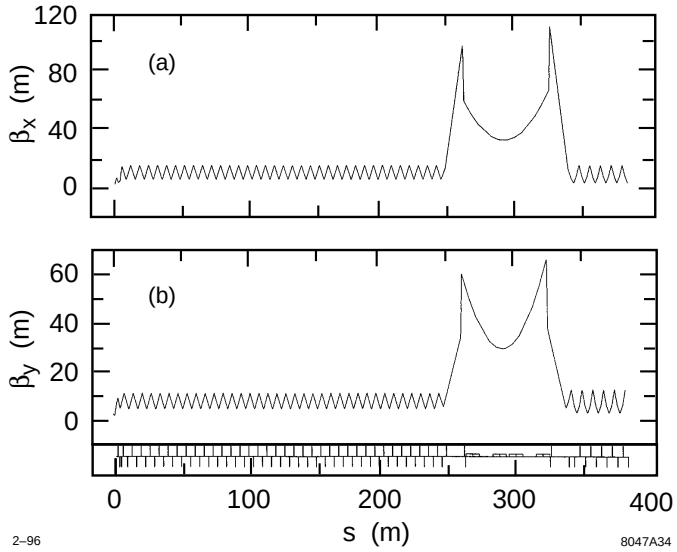

Figure 5-11. *Beta functions for chicane.*

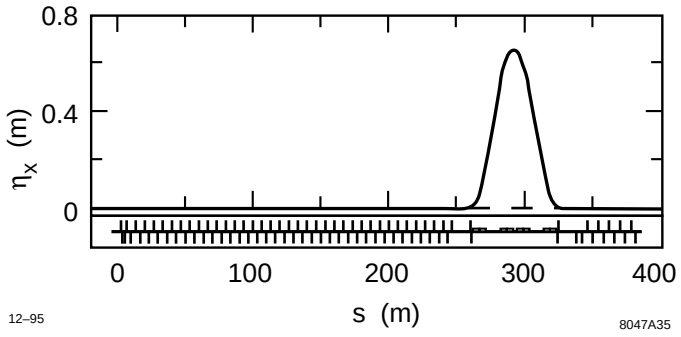

Figure 5-12. *Dispersion function for chicane.*

5.4 Longitudinal Dynamics

The primary purpose of the bunch compressor system is to rotate the longitudinal phase space from the damping rings by $\pi/2$ while compressing the bunch length. In this process, nonlinearities distort the phase space, changing the bunch shape and the sensitivity to incoming phase errors from the damping rings. In this section, we discuss the sources of nonlinearity and their compensation and we present simulation results illustrating the longitudinal beam distributions at the IP.

Finally, it should be noted that most of these simulations were performed before the structure parameters were finalized. Thus, the wakefields that were used in the simulations are stronger than those expected and only the ΔF technique was used for the beam loading compensation. Both of these differences will cause the simulations to *overestimate* the sensitivities and errors. Since this document is primarily a feasibility study and the feasibility is clearly demonstrated, we have not yet re-calculated the effects.

5.4.1 Optical and RF Nonlinearities

Having been given all parameters as described and having generated the desired linear transfer matrix for the longitudinal phase space, the tracking simulations still show a fairly large variation of rms energy spread, and, in particular, of the mean energy at the end of the main linac as a function of initial phase error. For instance, a 6-mm initial phase error causes a change of the final beam energy by about 0.2%–0.3%, which is too large to be tolerable. Furthermore, the mean energy and energy spread show a very asymmetric dependence on positive and negative phase errors.

An important nonlinear aberration of the system is due to the quadratic dependence of the final longitudinal phase on the incoming energy (the T_{566} transfer-matrix element in TRANSPORT notation [Brown 1977]) for the different subsystems. It is straightforward to see (compare Section 5.4.2) that for wiggler and chicane we have

$$T_{566}^{w,c} = -\frac{3}{2} R_{56}^{w,c} \tag{5.23}$$

while for the present lattice of the arc we find

$$T_{566}^{a} \approx 1.9 \cdot R_{56}^{a} \quad . \tag{5.24}$$

It is the nonzero $T_{566}^{w,c}$ coefficient of wiggler and chicane which causes the intolerably large variation of the final energy at the end of the main linac as a function of initial phase error. (The T_{566}^{a} of the arc is not significant.)

There are two effects that are important. First, initial phase errors give rise to energy errors δ_1 after the first compressor rf, which in turn, due to the T_{566}^{w} of the wiggler, cause a phase offset in the prelinac. The result is an additional energy change $\Delta\delta_{pl}$ which may either add to or cancel the energy error δ_1, dependent on the sign of the offset. The second compressor further enhances the energy error and, due to the T_{566}^{c} of the chicane, generates a significant phase error in the main linac. A second effect is that, if the bunch is longitudinally off-set, the T_{566} can either increase or counteract the nonlinearity of the rf, giving rise to an asymmetry in bunch length versus phase error, for each compressor stage separately.

The simulation results show that it is desirable to compensate the sensitivity to initial phase errors caused by the $T_{566}^{w,c}$ of wiggler and chicane. A compensation can be performed, for instance, with an additional, decelerating rf [Raubenheimer 1994b], whose purpose is to cancel the quadratic dependence of the final phase z_f on the longitudinal position (the phase error) at the compressor rf. Consider the main compressor rf

$$V \cos(\psi + kz) \tag{5.25}$$

and a compensating rf

$$V_c \cos(\psi_c + k_c z) \tag{5.26}$$

with V_c small compared with the beam energy E, $V_c \ll E$, followed by a chicane or a wiggler. The phase z_f at the exit of this system depends on the initial phase z_{rf} at the rf as

$$\begin{aligned} z_f &= (1 - R_{56}^{w,c}(f + f_c)) z_{rf} + T_{566}^{w,c}(f + f_c)^2 z_{rf}^2 \\ &\quad + \frac{1}{2} R_{56}^{w,c}(fk \cot\psi + f_c k_c \cot\psi_c) z_{rf}^2 \end{aligned} \tag{5.27}$$

where we have omitted a constant shift as well as higher-order terms, $f_c \equiv V_c k_c \sin\psi_c/(E + V\cos\psi)$ for the compensating rf, and $f \equiv Vk \sin\psi/(E + V\cos\psi)$ is the corresponding value for the main compressor rf; $k \equiv 2\pi/\lambda$ is the wave number. The sum of the quadratic terms in Eq. 5.27 is zero if we choose

$$T_{566}^{w,c}(f + f_c)^2 = \frac{1}{2} R_{56}^{w,c}(fk \cot\psi + f_c k_c \cot\psi_c) \tag{5.28}$$

which, for the special case $\psi = -\pi/2$ and $\psi_c = \pi$, simplifies to

$$V_c = -2\frac{T_{566}^{w,c}}{R_{56}^{w,c}}\frac{k^2V^2}{k_c^2E} = 3\frac{\lambda_c^2V^2}{\lambda^2E} \tag{5.29}$$

where we have used Eq. 5.23. Alternately, assuming no additional compensating rf system and only changing the rf phase, we find:

$$\cot(\psi) = 3\frac{f}{k} \quad . \tag{5.30}$$

In the first compressor stage, we can simply change the L-band rf phase from $-90°$ to $-101°$ to perform the compensation. Unfortunately, in the second compressor this is more difficult; the S-band rf would have to be run roughly $-50°$ from the zero crossing to provide sufficient curvature. Instead, we plan to use 275 MV of X-band rf operating at a phase of $-180°$ to perform the compensation.

With the compensation, the residual longitudinal aberrations are now third order and higher. An initial phase error or multibunch beam loading may cause an energy offset δ of the entire bunch at the entrance to the high-energy compressor (BC2). In addition, the longitudinal wakefields in the prelinac induce a (mainly) quadratic δ-z-correlation, where z is the longitudinal position of a single particle with respect to the bunch center. Due to the R_{56}^a of the arc, this energy error translates into a position error at the two rf systems of BC2, which is transformed once more into energy by the rf, and back into longitudinal phase by the T_{566}^c of the chicane. The final phase z_f of a single particle at the exit of BC2 is

$$z_f \approx az - bz^4 - c\delta^2z^2 - d\delta z^2 - e\delta z^4 + \ldots \tag{5.31}$$

where $a \approx 1/5$–$1/7$ is the desired linear compression ratio, and the four nonlinear terms on the right-hand side are about the same size (10–20 μm), for typical values $\delta \approx \pm 0.004$ and $z \approx 500\,\mu$m. These four terms are negligibly small if the prelinac wakefields are absent.

5.4.2 The T_{566}-Matrix Element

Let the trajectory of an arbitrary particle be described by a general dispersion function η as $x = \eta\delta$, where δ is the relative momentum deviation. The dispersion function may be expanded as a power series in δ:

$$\eta\delta = \eta_0\delta + \eta_1\delta^2 + \ldots \tag{5.32}$$

For a system of bending magnets and quadrupoles with bending radius ρ and gradient k, the functions η_0 and η_1 fulfill the differential equations [Delahaye 1985]

$$\eta_0'' + \left(\frac{1}{\rho^2} + k\right)\eta_0 = \frac{1}{\rho} \tag{5.33}$$

$$\eta_1'' + \left(\frac{1}{\rho^2} + k\right)\eta_1 \approx -\frac{1}{\rho} + \left(k + \frac{2}{\rho^2}\right)\eta_0 \tag{5.34}$$

which, for $\eta_0 \ll \rho$, may be further approximated by

$$\eta_0'' + k\eta_0 \approx \frac{1}{\rho} \tag{5.35}$$

$$\eta_1'' + k\eta_1 \approx -\frac{1}{\rho} + k\eta_0 \tag{5.36}$$

The R_{56}- and T_{566}-matrix-elements may be expressed in terms of $\eta_{0,1}$ [Delahaye 1985]

$$R_{56} = -\int \frac{\eta_0}{\rho} ds \tag{5.37}$$

$$T_{566} \approx -\int \left(\frac{\eta_1}{\rho} + \frac{1}{2}\eta_0'^2 \right) ds \tag{5.38}$$

In case of wiggler and chicane $k\eta_{0,1} = 0$ and, therefore, $\eta_1 = -\eta_0$. Since $\eta_0'' \approx 1/\rho$, the second term in the expression for T_{566} can be integrated by parts, with the final result

$$T_{566} \approx -\frac{3}{2} R_{56} \qquad \text{(for wiggler and chicane)} \quad . \tag{5.39}$$

To reduce the T_{566}-matrix-element, the value of the second-order dispersion needs to be reduced. Ideally, one would like to have $T_{566} = 0$, which requires a sign reversal of η_1 such as to cancel the contribution from $\eta_0'^2$. This can be accomplished by adding quadrupoles at locations with nonzero η_0, as evident from Eq. 5.36, or by adding sextupoles (not included in the above equations). Unfortunately, such changes to η_1 may adversely affect the transverse emittances.

5.4.3 Single Bunch Longitudinal Wakefields

Longitudinal wakefields in the S-band accelerator seriously modify the longitudinal phase space. For our calculations we have assumed the SLAC wakefield. The actual wakefield for the NLC will be roughly $\sqrt{2}$ smaller because of the increased iris aperture. Thus, we have over-estimated the tolerances and sensitivities.

5.4.4 Multibunch Wakefields

Thus far, the simulations have included only the fundamental longitudinal mode for the different S-band, L-band, and X-band rf sections. Parameters were provided by R. Miller [Miller 1995] and are listed in Table 5-6; these parameters differ slightly from the structure design parameters described in Chapter 6.

5.4.5 Bunch Shaping

At this time, we have not investigated the option of deliberately shaping the longitudinal profile of the bunch to reduce the energy spread induced by the longitudinal wakefields and/or the transverse emittance dilution. However, a two-stage bunch-length collimation section is part of the bunch-compressor and linac design; it is discussed in Chapter 9. This system, by itself, already reduces the beam energy spread, and it would be an integral part of any bunch-shaping strategy. More studies on this topic are left for the future.

5.4.6 Longitudinal Phase Space at the End of the Linac

To determine the optimum parameters of the system, we have considered four NLC scenarios, corresponding to different bunch lengths and energies (see Table 5-5). The parameters chosen enclose the NLC operating plane as described in Chapter 1.

	NLC-I		NLC-II	
Cms energy	500 GeV	500 GeV	1 TeV	1 TeV
Bunch length	100 μm	150 μm	125 μm	150 μm
Single-bunch gradient	33.25 MV/m	29.13 MV/m	60.19 MV/m	53.97 MV/m
$L_{\rm acc}$	8130 m	8130 m	8900 m	8900 m
N/bunch (10^{10})	0.65	0.85	0.95	1.25
$E_{\rm max}$ (GeV)	267	233	534	473
Average $\phi_{\rm rf}$ ($^\circ$)[a]	-14.4	-15.1	-7.2	-11.0

[a] with respect to beam center, for 0.8% FWHM energy spread.

Table 5-5. *Four different NLC scenarios considered in the bunch-compressor simulations.*

Computer simulations of the longitudinal single-bunch dynamics have been performed with the code LITRACK [Bane]. In these simulations, a distribution of particles as extracted from the damping rings is tracked through the different compressor subsystems and the main X-band linac. The parameters of the bunch compressor are optimized such that the final average energy and the energy spread at the end of the main linac are insensitive (*i.e.*, vary by less than 0.1%–0.2%) to initial phase errors up to 20° S-band, or ± 6 mm.

In the latest simulation studies, the phase of the main X-band linac was adjusted to obtain a final full-width, half-maximum (FWHM) energy spread of about 0.8%. This energy spread is slightly smaller than the energy bandwidth of the final focus (see Chapter 11) and it might be reduced further by tuning the rf properties in the X-band linac. Figures 5-13 through 5-16 present tracking results for two different bunch lengths in either NLC-I and NLC-II. Shown is the longitudinal distribution at the exit of the bunch compressor and, for five different initial phases, at the end of the main linac. Figure 5-17 presents the dependence of the average energy on the initial phase error, for the same four NLC scenarios. Figures 5-18 and 5-19 show equivalent pictures for the rms and FWHM energy spread, respectively. In all cases, the beams are acceptable for the final focus.

5.4.7 Multibunch Dynamics

The real purpose of the bunch compressors is not to reduce the length of a single bunch, but the length of each bunch in the train of 90 bunches. This task is complicated by the longitudinal long-range wakefields and the pertinent multibunch beam loading in the various accelerator sections of the compressor.

In this section, we will evaluate the ΔF compensation technique for the multibunch beam loading which adds two additional rf systems with slightly different frequencies to each acceleration section [Kikuchi 1992]. These rf systems generate an additional voltage which increases almost linearly along the bunch train, and which can be adjusted to cancel the linear part of the multibunch beam loading. It should be noted that the present rf system design actually uses a combination of ΔT and ΔF techniques that is much more effective than just the ΔF technique described here.

A simulation study has been performed to test this multibunch energy compensation scheme and the interplay of longitudinal single- and multibunch dynamics in the bunch compressor. For the purpose of this study, the long-range wakefields have been confined to the fundamental mode. The wakefield of a structure is then characterized by three numbers: the loss factor k, the mode frequency f, and the quality factor Q. In terms of these quantities, the wakefield at a distance z reads

$$W(z) = 2k\cos\left(\frac{2\pi f z}{c}\right) e^{-\frac{2\pi f z}{2Q}} \tag{5.40}$$

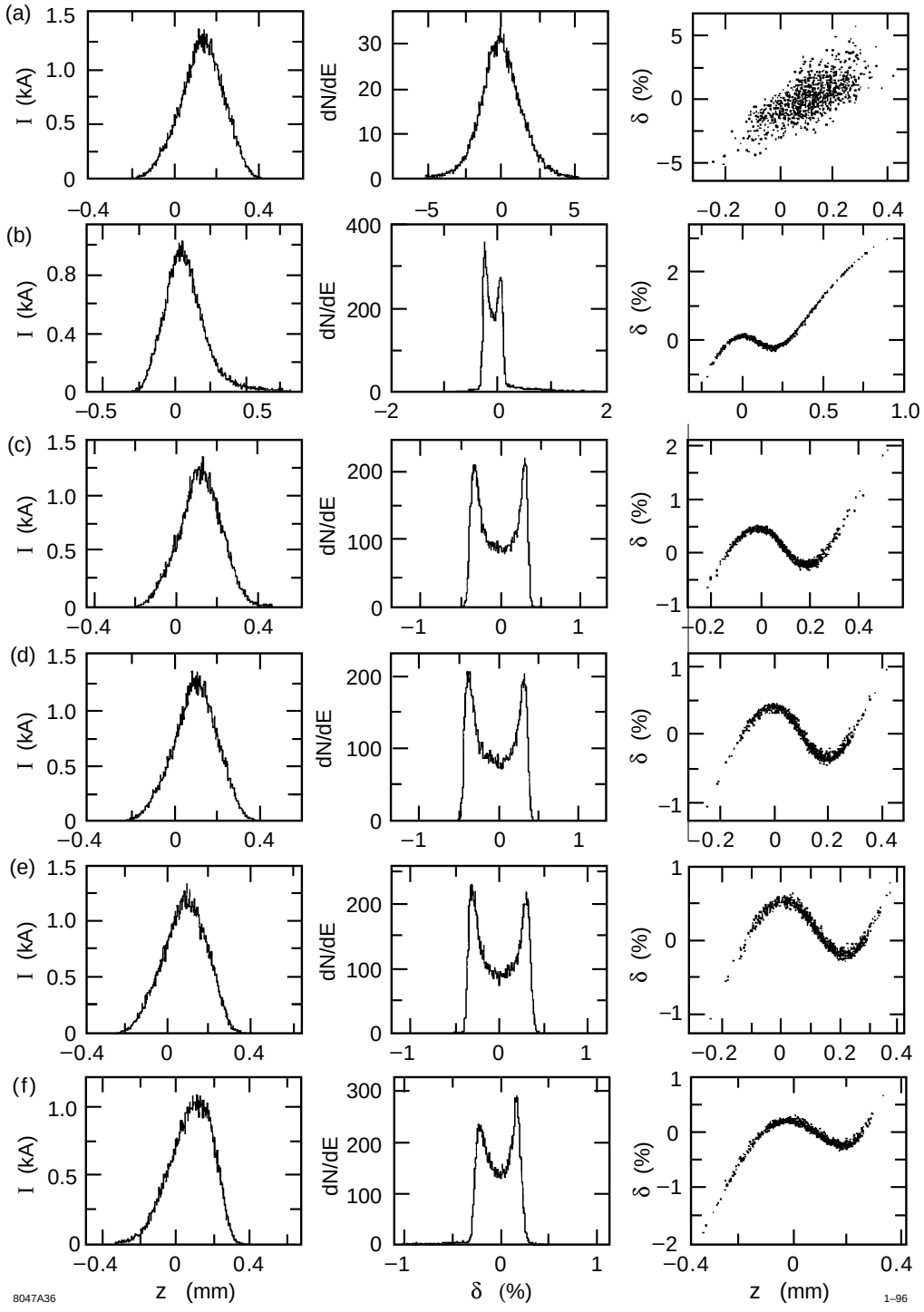

Figure 5-13. *Longitudinal phase space distributions for NLC-Ia, $N = 6.5 \times 10^9$ and a final bunch length of 100 μm: a) after the bunch compressor; and at the end of the main linac for an initial phase error of b) −12, c) −6, d) 0, e) 6, f) 12 mm.*

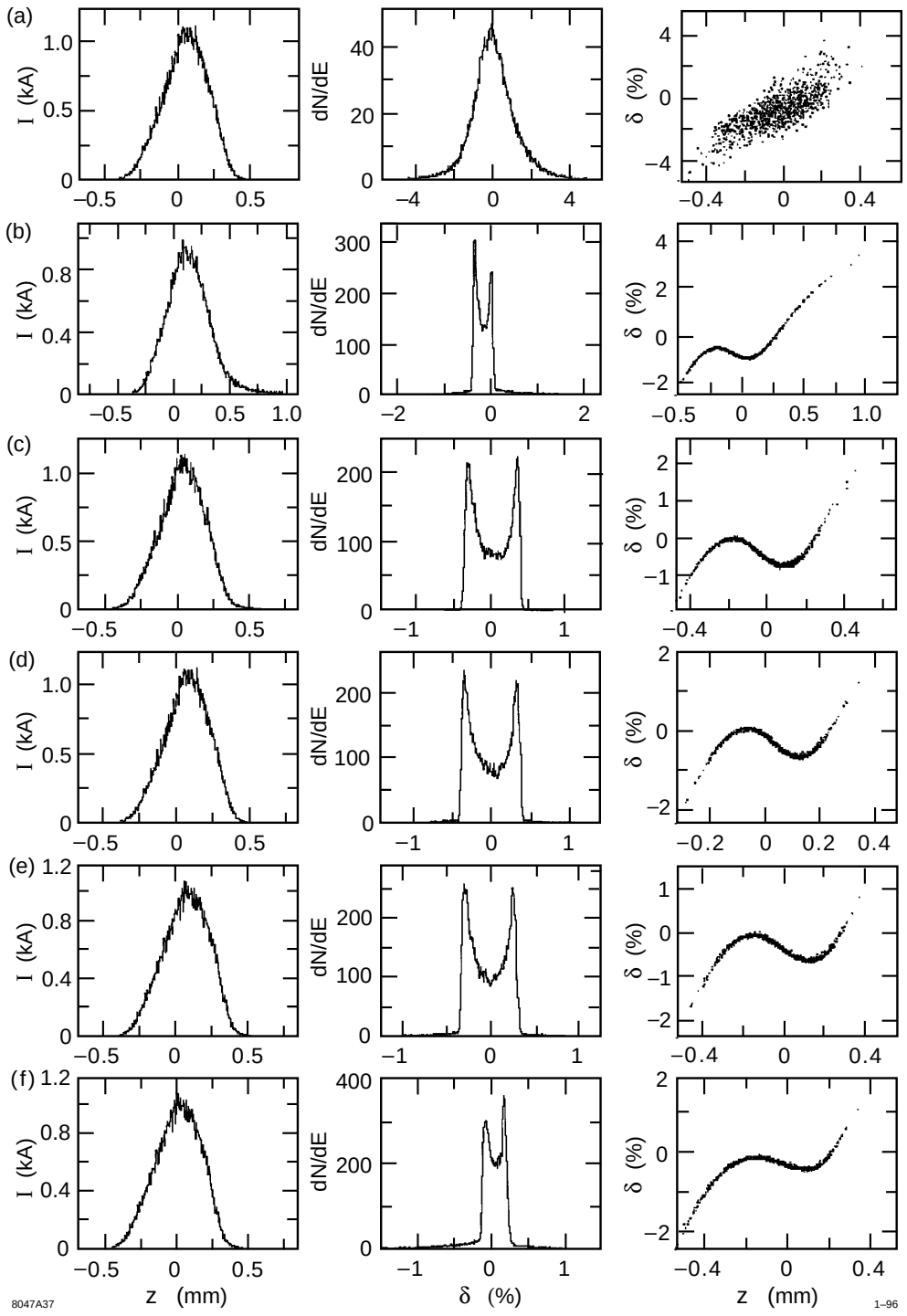

Figure 5-14. *Longitudinal phase space distributions for NLC-I c, $N = 8.5 \times 10^9$ and a final bunch length of 150 μm: a) after the bunch compressor; and at the end of main linac for an initial phase error of b) – 12, c) – 6, d) 0, e) 6, f) 12 mm.*

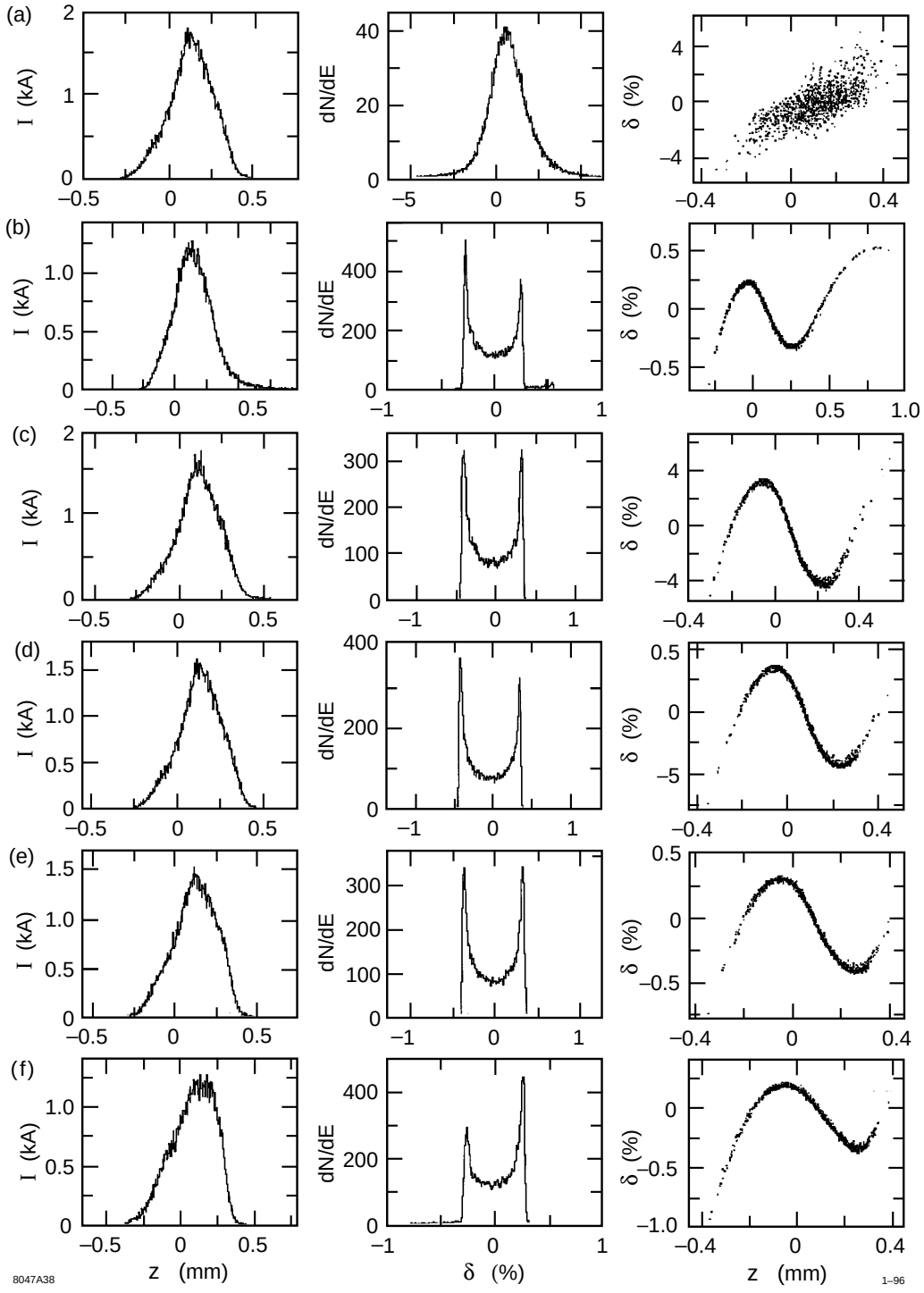

Figure 5-15. *Longitudinal phase space distributions for NLC-IIa, $N = 9.5 \times 10^9$ and a final bunch length of 125 μm: a) after the bunch compressor; and at the end of the main linac for an initial phase error of b) −12, c) −6, d) 0, e) 6, f) 12 mm.*

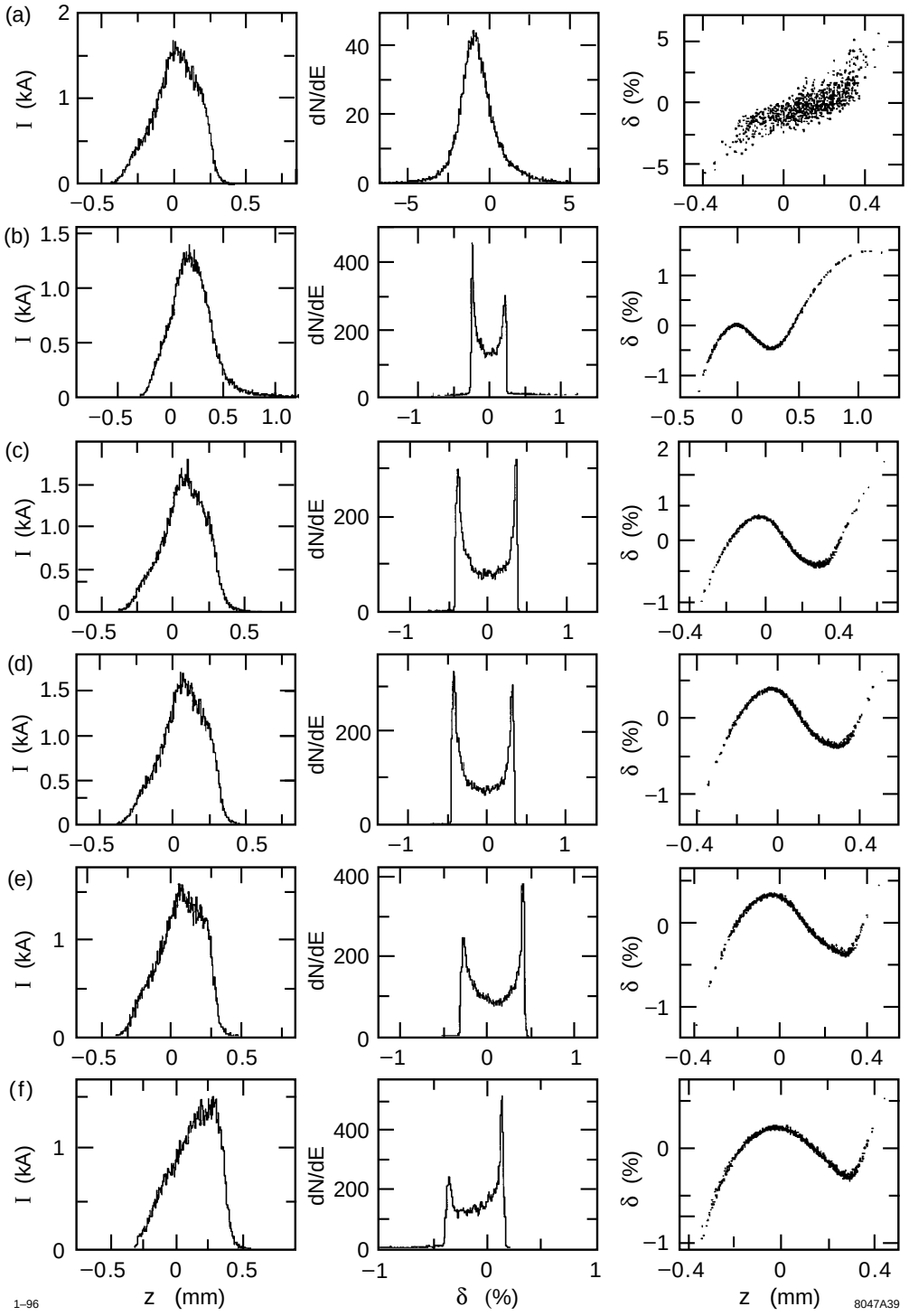

Figure 5-16. *Longitudinal phase space distributions for NLC-IIc, $N = 1.25 \times 10^{10}$ and a final bunch length of 150 μm: a) after the bunch compressor; and at the end of the the main linac for an initial phase error of b) −12, c) −6, d) 0, e) 6, f) 12 mm.*

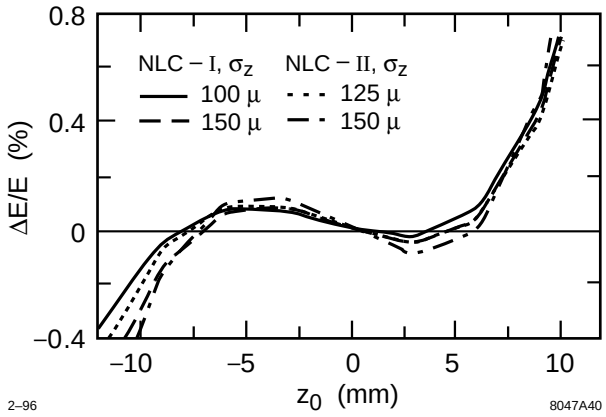

Figure 5-17. *Variation of average energy with initial phase error, for two different bunch lengths in the NLC-I and NLC-II.*

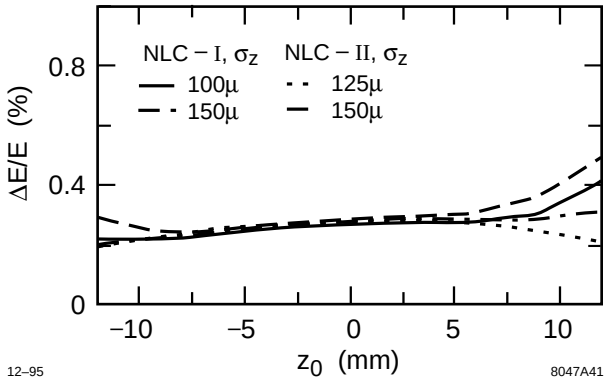

Figure 5-18. *Variation of rms energy spread with initial phase error, for two different bunch lengths in the NLC-I and NLC-II.*

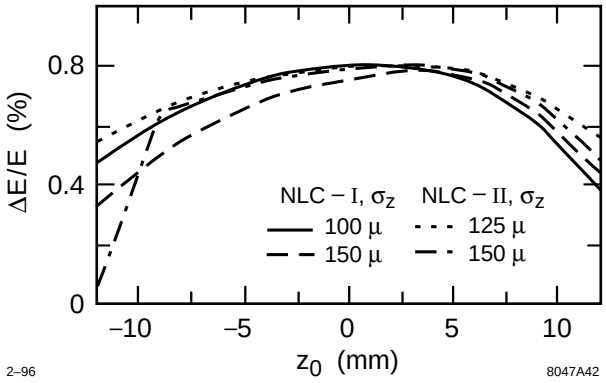

Figure 5-19. *Variation of FWHM energy spread with initial phase error, for two different bunch lengths in the NLC-I and NLC-II.*

Parameter	L-Band	S-Band	X-Band	Comment
f (GHz)	1.428	2.856	11.424	frequency
$2\,k$ (V/C/ m)	1.8×10^{13}	3.7×10^{13}	2.0×10^{14}	loss factor $\times$ 2
v_g/c	0.012	0.012	0.08	group velocity
Q	18, 000	13, 000	7000	quality factor
l (m)	6	3	1.8	structure length

Table 5-6. *Wakefield and structure parameters for the different accelerating sections in the bunch compressor.*

where c denotes the velocity of light. Also taken into account in the simulation is the group velocity of the fundamental mode, which introduces a small nonlinear component to the beam loading and makes perfect beam-loading compensation impossible—at least for the compensation scheme presently chosen. Wakefield parameters for the different structures were provided by R. Miller [Miller 1995]. They are compiled in Table 5-6.

The short-range wakefields used in the multibunch simulations are the same as those which were employed in the single-bunch case: The short-range wakefield for the X-band structure was derived by K. Bane [Bane 1995]. The wakefields for other frequencies were estimated from an approximative formula in Ref. [Palmer 1990].

The multi-bunch energy compensation scheme of choice was proposed by Kikuchi [Kikuchi 1992]. If two rf structures are driven at frequencies $f_0 \pm \Delta f$, the effective total voltage for the nth bunch is

$$\Delta V_n = V_c \sin\left(\frac{2\pi(f_0+\Delta f)z_n}{c}\right) - V_c \sin\left(\frac{2\pi(f_0-\Delta f)z_n}{c}\right) \tag{5.41}$$

$$\approx 4\pi V_c \frac{\Delta f}{c} \cos\left(\frac{2\pi f_0 z_n}{c}\right) \tag{5.42}$$

where z_n denotes the longitudinal position of the bunch, and $2\pi\ \Delta f z_n/c \ll 1$ was assumed. The required compensation voltage V_c is [Kikuchi 1992]

$$V_c = qc\frac{k_m L_m + 2k_c L_c}{b\ 2\pi\Delta f} \tag{5.43}$$

where $(k_m L_m)$ and $(2k_c L_c)$ are the beam-loading voltage in the main rf structure and compensating cavities, respectively, and b is the bunch spacing.

For all subsystems a compensation frequency in the S-band region was chosen, detuned from the main S-Band frequency by $\Delta f \approx \pm 1$ MHz. Several considerations determined the optimum choice of Δf. In general, a larger Δf reduces the required compensation voltage and the additional beam loading. The compensation, however, becomes less linear for larger beam frequency. It seems best to choose the frequency difference so as to partially cancel the nonlinear component of the beam loading. In the simulation, this is done empirically by minimizing the rms energy variation (or phase variation) as a function of Δf.

The initial setup of the multibunch compensating rf was performed by considering only one macroparticle per bunch in order to increase the computational speed. Subsequently, the main rf-voltages and phases were re-optimized for the single-bunch dynamics. This is necessary because of additional short-range wakefields in the compensation structures. Finally, a train of 90 bunches, 50 macroparticles each, was tracked through the entire system, and through the X-Band main linac. No long-range wakefields in the X-Band linac were considered, assuming that they are perfectly compensated by rf-pulse shaping.

The simulation includes an initial linear phase variation of ± 3 mm along the bunch train, as caused by beam loading in the damping rings. There is no need for a particular rf system to compensate this initial phase variation, since the compressor was designed to handle single-bunch phase errors up to ± 6 mm or larger.

Table 5-7 summarizes the compressor parameters used in the simulation. Note that the active length of the prelinac is about 320 m, and thus about 30% shorter than in the present ZDR design. The 320-m length assumes an unrealistic gradient of 30 MV/ m (or up to 36 MV/ m for the compensating rf) but the performance is not expected to be much different for a greater length.

Results of the simulation study are summarized in Figures 5-20 and 5-21 and in Table 5-8. Note that the bunch-to-bunch variation of energy, position, and bunch length, apparent in the two figures, arises from the finite number of macroparticles per bunch (50), and is much larger than the expected actual bunch-to-bunch variation. On the other hand, the slow change of energy, position, and bunch length over several bunches represents the effect of the long-range wakefields, and is the quantity of interest here. Table 5-8 lists the longitudinal bunch-to-bunch phase variation, the bunch-to-bunch energy spread, the intrabunch energy spread, and the rms bunch length at the end of the main linac, for different NLC scenarios. The longitudinal bunch position varies by 30–40 μm about the average value. The bunch length fluctuates by ± 10 μm. Changes of phase and bunch length give rise to a bunch-to-bunch rms energy variation of roughly 0.1–0.2%, and a total variation of 0.8% for the NLC-I and 0.6% for the NLC-II. The rms intrabunch energy spread is 0.3–0.4% in all cases.

We conclude that the ΔF multibunch energy compensation is straightforward and, in the simulation, its performance is adequate and satisfactory. The primary disadvantage of the ΔF technique is that the compensation is not local and thus the dispersive and chromatic emittance dilutions are larger. In the NLC injectors, we have adopted a combination of the ΔT and ΔF techniques that should perform far better than the ΔF scheme reported here–this is described in Chapter 6.

Parameter	Collider Version NLC-Ia	NLC-Ic	NLC-IIa	NLC-IIc	Comment
V_{LB} (MV) ϕ_{LB} (°) L (m)	136.0 −89.88	136.5 −89.88	136.0 −89.92 8.5	136.0 −89.88	Main L-band RF 1st stage $f = 1.428$ GHz
V_{SB} (MV) ϕ_{SB} (°) L (m)			6.9 −180.0 0.4		Comp. S-band RF 1st Stage $f = 2.856$ GHz
V_{SB} (MV) Δf (kHz) ϕ_{SB} (°) L (m)	±26.7	±34.4	±38.4 ± 856.8 −90. 2×3.0	±50.5	Multibunch Comp. S-band RF 1st Stage $f_c = f_0 \pm \Delta f$, $f_0 = 2.856$ GHz
V_{SB} (MV) ϕ_{SB} (°) L (m)	8050 −4.0	8049 −3.0	8054 −3.0 270	8068 −3.0	Prelinac S-Band RF $f = 2.856$ GHz
V_{SB} (MV) Δf (kHz) ϕ_{SB} (°) L (m)	±805	±1037	±1159 ± 856.8 −90. 2×27 / 2×39	±1525	Multibunch Comp. S-band RF Prelinac $f_c = f_0 \pm \Delta f$, $f_0 = 2.856$ GHz
V_{SB} (MV) ϕ_{SB} (°) L (m)	3850 −89.6	3500 −88.5	3730 −89.7 130	3610 −89.7	Main S-band RF 2nd Stage $f = 2.856$ GHz
V_{XB} (MV) ϕ_{XB} (°) L (m)	274	276	256 −183.0 8	240	Comp. X-band RF 2nd Stage $f = 11.424$ GHz
V_{SB} (MV) Δf (kHz) ϕ_{SB} (°) L (m)	±338	±440	±492 ± 1142.4 −90. 2×15.0	±647	Multibunch Comp. S-band RF 2nd stage $f_c = f_0 \pm \Delta f$, $f_0 = 2.856$ GHz
V_{XB} (GV) ϕ_{XB} (°) L (m)	270.32 −15.7 8130	236.83 −16.1 8130	535.69 −8.3 8900	480.33 −12.0 8900	Main Linac X-band RF $f = 11.424$ GHz

Table 5-7. *Rf parameters of compressor subsystems, as used in the multibunch simulation study.*

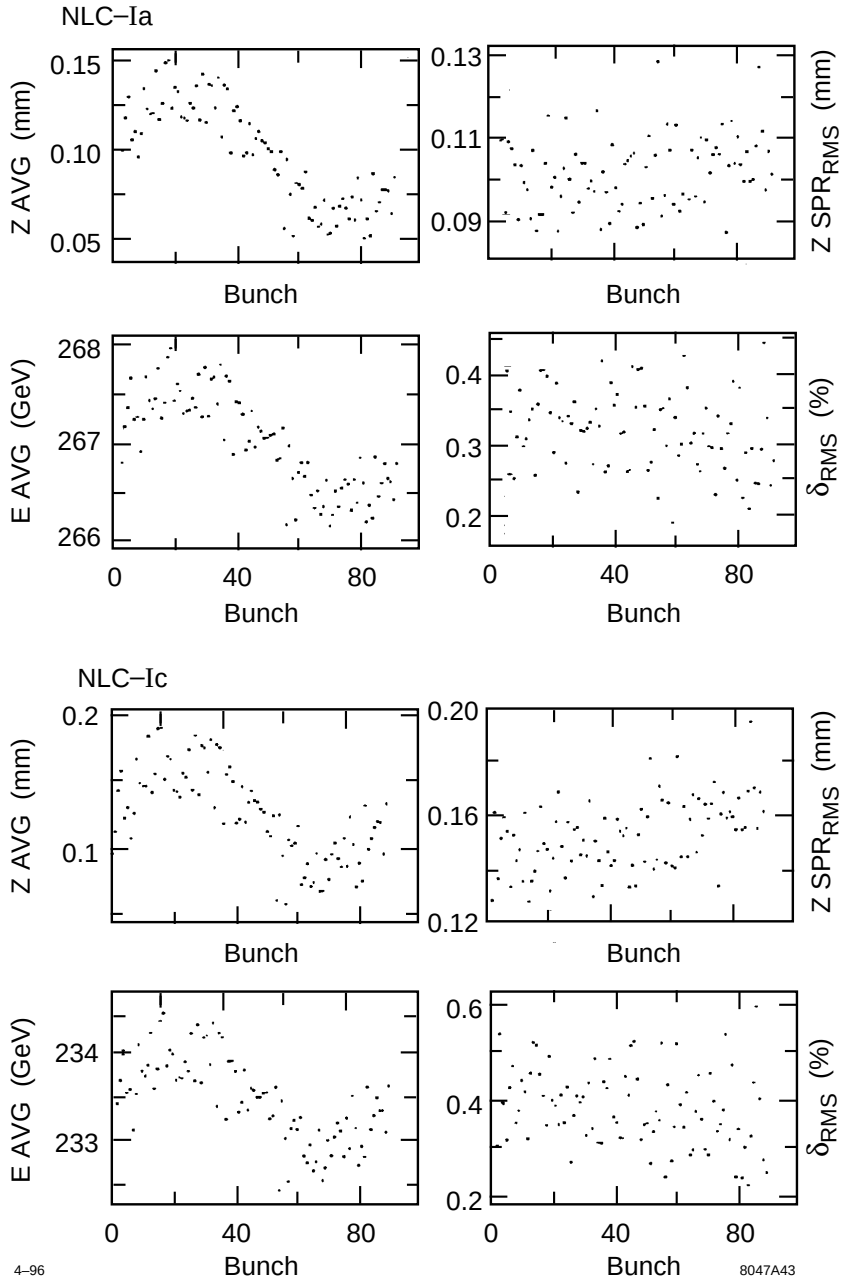

Figure 5-20. *Bunch centroid position, rms bunch length, average bunch energy, and rms energy spread, as a function of bunch number in a train of 90 bunches, for two different versions of NLC-I.*

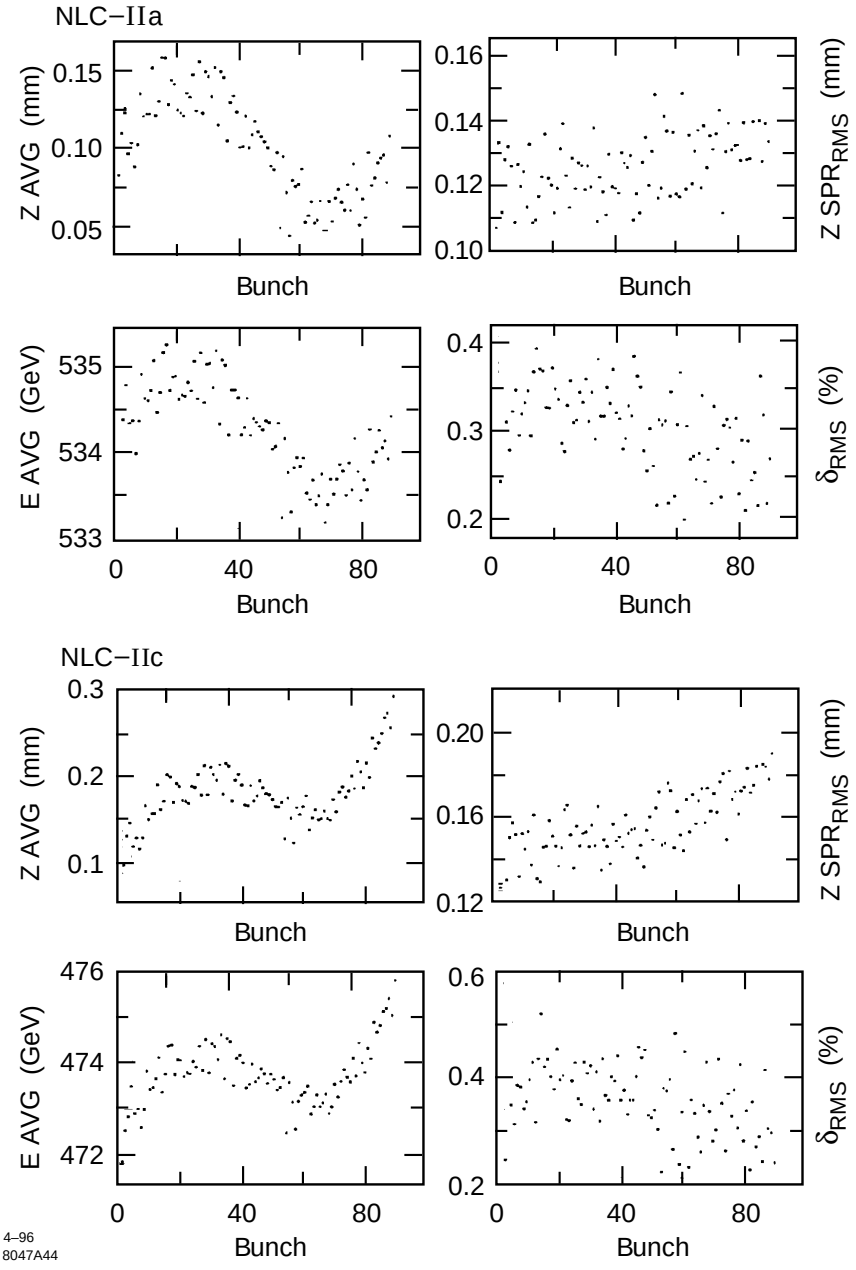

Figure 5-21. *Bunch centroid position, rms bunch length, average bunch energy, and rms energy spread, as a function of bunch number in a train of 90 bunches, for two different versions of NLC-II.*

Parameter	Collider Version				Comment
	NLC-Ia	NLC-Ic	NLC-IIa	NLC-IIc	
$z_{b,\ rms}$ (μm)	28	33	31	36	Rms phase variation
$\sigma_{z,\ ave}$ (μm)	100 ± 9	153 ± 13	125 ± 10	156 ± 15	Average bunch length
$\delta_{b,\ rms}$ (%)	0.18	0.20	0.09	0.14	Rms energy variation
$\sigma_{\delta,\ ave}$ (%)	0.31	0.38	0.31	0.36	Intrabunch rms energy spread
E_b (GeV)	266.9	233.46	534.2	473.7	Average energy

Table 5-8. *Inter- and intrabunch energy spread, rms bunch length, and longitudinal phase variation at the end of the X-band main linac, for a train of 90 bunches in two different versions of the NLC-I and NLC-II. Numbers were obtained by a macroparticle simulation, which includes the effect of short- and long-range wakefields, multibunch energy compensation, and an initial phase variation of 6 mm along the train.*

5.5 Transverse Dynamics

In this section, we will examine the effects that can dilute the transverse emittances. The primary source of dilution are optical aberrations in the spin rotator and compressors and single bunch wakefields in the linacs. We will describe these effects and the respective tuning compensation systems in three regions which are organized according to the respective diagnostic sections. Thus, we will describe the tuning in the spin rotator and low-energy bunch compressor, in the prelinac, and in the high-energy bunch compressor. Next, we will discuss the effect of the multibunch transverse wakefields and then finally we will describe the effects of: space charge fields and coherent radiation, ion trapping, and synchrotron radiation. All of these later effects impose weak constraints on the system design.

5.5.1 Spin Rotator and Low-Energy Bunch Compressor

Given the small vertical emittance at damping ring extraction ($\gamma\epsilon_y = 3 \times 10^{-8}$ m), it is crucial that tuning elements and algorithms be provided which will allow full correction of the inevitable fabrication and alignment errors of the first bunch compressor (BC1). This is especially necessary when considering the large energy spread incurred after the BC1 rf structures ($\sim$1% rms) as well as the large cross-plane coupling generated and canceled again between spin rotator solenoids. The following section describes dispersion correction elements, coupling correctors, beam matching, and diagnostics necessary for preserving the damped transverse emittance. In addition, the results from a full tuning simulation are presented.

Tuning Elements and Aberrations

Dispersion Correction Elements. The large energy spread of the bunch compressor sets very tight tolerances on residual dispersion, especially in the vertical plane. The relative emittance dilution due to residual spatial, η, and angular, $\eta\prime$, dispersion is expressed in Eq. 5.44 including subsequent chromatic filamentation.

$$\frac{\delta\epsilon}{\epsilon_0} = \frac{\eta^2 + (\eta\alpha + \eta\prime\beta)^2}{2\epsilon_0\beta}\sigma_\delta^2 \quad . \tag{5.44}$$

The tolerable vertical spatial dispersion at a point $\beta = 10\,\mathrm{m}, \alpha = 0$, is 175 μm (2% emittance dilution at $\gamma\epsilon_y = 3 \times 10^{-8}$ m and 1% rms energy spread). To correct at this level, four small skew quadrupoles are placed in the wiggler section of the BC1 at points of large horizontal dispersion. These are tiny correction elements (10-cm long, 30-mm pole-tip radius, $\pm$1 kGauss pole-tip field). They are paired at $-I$ (transfer matrix) intervals so that coupling is not generated and the pairs are separated by 90°. In this way, orthogonal η and $\eta\prime$ knobs are available. A similar system of four normal quadrupoles is used for horizontal dispersion correction. Figure 5-22 shows the placement of these skew and normal elements (SQW1,...4, CQW1,...4), as well as other elements discussed below.

In addition to dispersion correction after the BC1 rf structures, it is useful to include two more skew quadrupoles (SQR1, SQR2) in the mini-arc section of the spin rotator to provide correction of residual vertical dispersion generated before the rf sections. The net emittance dilution is a linear combination of the two residual dispersion functions weighted by their respective energy spreads (1% post-compression and 0.1% pre-compression). Although post-compression dispersion is much more intolerable, any significant pre-compression dispersion will not be correctable by the wiggler section skew quadrupoles. The two skew elements in the mini-arc are separated by 90° to provide spatial and angular pre-compression vertical dispersion correction. The ratio $(\eta_x\sigma_\delta)^2/\beta_x\epsilon_x >> 1$ so that paired coupling cancelation is not necessary.

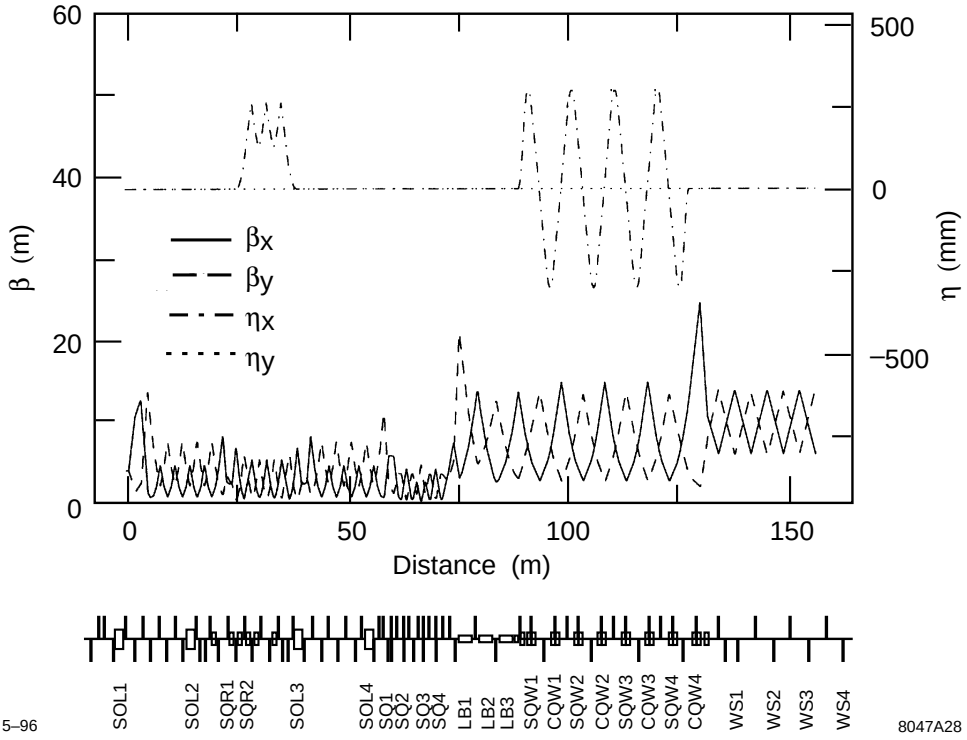

Figure 5-22. *Dispersion and beta functions for the entire low-energy bunch compressor and spin rotator system. Tuning elements and major component locations are indicated.*

Coupling Correction. The spin rotator solenoids (SOL1,...4) are nominally separated by optics which will cancel their cross-plane coupling. However, imperfections in the cancelation optics will result in emittance dilution. Furthermore it may be necessary to correct coupling generated within the damping rings. Therefore, a skew correction section is included following the spin rotator. This section contains four skew quadrupoles (SQ1,...4) in a non-dispersive section which is placed at ideal phase advance points so that they are initially orthonormal. The vertical emittance is minimized with each of these four skew elements. At the end of this process, and allowing for some reiteration, the coupling is completely corrected.

Beam Matching. Several provisions exist in the BC1 to compensate for matching errors. There are four variable strength quadrupoles which match the extracted beam to the spin rotator optics. There are also matching quadrupoles within the spin rotator to compensate for the focusing effect of the solenoids. Finally there are several matching quads between the skew correction section and the wiggler and also after the wiggler section. The BC1 rf may be switched off in order to distinguish more clearly between dispersion errors and matching errors.

Second-Order Corrections. Although it is not necessary to include local sextupole chromatic corrections for the design optics, simulations have shown (Section 5.5.1, Tuning Simulations) that for large vertical dispersion corrections $(\epsilon_y/\epsilon_{y0} >> 10)$ some second-order dispersion arises. If this situation develops, it is a simple matter to include four skew sextupoles adjacent to the wiggler skew quadrupoles to provide T_{366} and T_{466} knobs which are paired so that vertical chromaticity is not generated.

RMS Quadrupole Strength Errors ($\Delta k/k$)	1.0%
RMS Dipole Magnet Roll Errors (θ)	0.25°
Initial Cross-Plane Coupling (DR output)	$\epsilon_y/\epsilon_{y0} = 2.2$
All Four Solenoids at Full Field	35 kGauss

Table 5-9. *Errors and conditions for bunch compressor and spin rotator tuning simulations.*

Phase Space Diagnostics. To measure the BC1 extracted beam, four wire scanners (WS1,...4) are placed at ideal phase advance intervals (45°) at the end of the wiggler. The corrections described above are applied by minimizing the measured emittance. It is not necessary to actually measure the cross-plane coupling. It is fully corrected by minimizing the projected vertical emittance. The matched beam size is the same at each wire ($\sim$10 μm vertically by $\sim$65 μm horizontally) and therefore the matched condition is easily recognizable. Wire scanner roll tolerances are readily achievable ($\sim 1°$). In addition, a wire scanner placed at a high-dispersion point ($\sim$220 mm) in the spin rotator mini-arc will be useful to measure the extracted damping ring energy spread ($\sim$0.1%). The ratio of the dispersive beam size to the betatron beam size is $\sim$4:1 here. Finally a wire scanner at a peak dispersion point ($\sim$240 mm) in the wiggler will be useful to measure the damping ring extracted bunch length (similar size ratio $\sim$4:1).

Tuning Simulations

Tuning simulations have been run for the many corrections described above using the *Final Focus Flight Simulator*. Table 5-9 summarizes the set of errors and conditions introduced to the bunch compressor and spin rotator system for these simulations.

These errors produce extreme conditions that result in a vertical emittance which is a factor of $>$200 times larger than the initial intrinsic emittance $\gamma\epsilon_{y0} = 2.3 \times 10^{-8}$ m. In this case, the vertical beam profiles measured on the wire scanners will increase from the nominal $\sim$10 μm to $>$130 μm.

The simulations are run to test the tuning algorithms, especially in this extreme case. In the tuning process, a realistic measurement resolution is not attempted. The emittance measurements are infinitely precise and the initial diluted vertical emittance is $\gamma\epsilon_{y0} = 540 \times 10^{-8}$ m. Although it may not be the optimal procedure, the following describes the tuning procedure used:

Step 1. With L-band rf switched on, scan both vertical dispersion knobs to minimize projected vertical emittance (some iteration useful at this extreme stage).

Step 2. With L-band rf switched on, scan both horizontal dispersion knobs to minimize projected horizontal emittance.

Step 3. With L-band rf switched off, scan the four coupling correction skew quadrupoles to minimize projected vertical emittance.

Step 4. With L-band rf switched off, match horizontal and vertical beta functions with damping ring extraction quadrupoles (not actually tested here).

Step 5. Repeat Steps 1 and 2 (most dilution caused by dispersion).

Step 6. With L-band rf switched on, scan both second-order vertical dispersion knobs to minimize projected vertical emittance (only necessary for these extreme conditions).

Step 7. With L-band rf switched off, scan pre-compression vertical dispersion knobs.

The simulation of this procedure with the conditions of Table 5-9 has proven very successful and results in a final emittance dilution of $<$2% in both planes. Quadrupole alignment errors were not included in the simulation; however,

this should simply add to vertical dispersion errors which are already extreme due to the large dipole magnet roll errors. It is estimated that such a procedure will probably require approximately 16 hours of real machine time.

5.5.2 Prelinac

The prelinac quadrupoles will be aligned using the standard quadrupole beam-based alignment procedure used in the main linacs and the beam-delivery sections. Each quadrupole will be powered with an individual power supply. Then, the power supply can be varied making it straightforward to determine the alignment of the quadrupole magnetic center with respect to the electrical center of the BPM captured in the magnet. Each quadrupole will be mounted on a remote magnet mover to facilitate the alignment. In addition, the accelerator structures will also be mounted on remote movers and will contain BPMs that will measure the induce dipole modes in the structures. This will allow the structure to be accurately aligned to the beam trajectory established by the quadrupoles. Finally, additional tuning, using oscillation bumps similar to those used in the SLC linac, could be performed using the emittance diagnostic station located at the end of the prelinac.

Simulations of the transverse emittance dilution were performed with the LInear Accelerator Research simulation program described in Chapter 7. In simulations, the residual vertical emittance dilution was less than 15% assuming errors due to 10 μm quad-BPM resolution, 40 μm structure BPM resolution, 200 μm initial quadrupole offsets, and 1 μm mover step size. The dilution is dominated by the dispersive dilution due to the large incoming energy spread (1%) of the beam. These are very loose tolerances. The expected errors are 2 μm quad-BPM misalignments, 20 μm structure BPM resolution, and 0.3 μm mover step size. These would yield a vertical emittance dilution that is less than 1%.

5.5.3 High-Energy Bunch Compressor

The high-energy bunch compressor can be separated into 3 stages: the 180° arc, the compressor rf, and the chicane. The quadrupoles in the arc and the compressor rf section will be aligned using the standard beam-based techniques that will also be used in the pre-linac, the main linac, and the beam-delivery section of the collider. Here, each quadrupole is powered with an individual power supply and the power supply is varied to determine the magnetic center of the quadrupole with respect to a BPM captured within the bore. The quadrupoles are then aligned with remote magnet movers; this algorithm is described in greater detail in Chapter 7. and the preceding section on the prelinac alignment. The arc was explicitly designed using separated function magnets to facilitate this form of alignment.

The 4-GeV compressor rf section has strong focusing to reduce the sensitivity to wakefields. To keep the vertical emittance dilution due to transverse wakefields to less than 1%, the accelerator structures must be aligned within 45 μm of the beam trajectory. This will be accomplished using structure BPMs ("S"-BPMs) to measure the induced dipole mode and the remote movers to align the structures to the beam path. Given this loose tolerance, no significant dilution is expected.

As in the low-energy bunch compressor, tuning elements must also be included in the high-energy compressor. The most likely mechanisms for emittance dilution are rolled dipoles and quadrupoles, misaligned quadrupoles and sextupoles, as well as quadrupole gradient errors, all of which generate mostly anomalous dispersion which phase mixes in the main linac (see Eq. 5.45). Cross-plane coupling and beta-mismatch errors are much less likely since the horizontal beam size in the arc and chicane is dominated by dispersion (*i.e.*, $\{\eta_x\sigma_\delta\}^2/\beta_x\epsilon_x \gg 1$) (see Table 5-4 and Figures 5-11 and 5-12). The next sections describe the tuning elements and algorithms for controlling anomalous dispersion in the arc and chicane; the tuning of the rf section was described earlier.

Name	Quantity	Roll (mrad)	$\Delta B/B_0$ (10^{-4})	b_1/b_0 (%)	b_2/b_0 (%)
BB	138	4.7	1.2	0.3	5

Table 5-10. *BC2 arc dipole magnet single element tolerances for 8% emittance growth each ($\gamma\varepsilon_{x0} = 3\times10^{-6}$ m, $\gamma\varepsilon_{y0} = 3\times10^{-8}$ m, $\sigma_\delta = 0.25\%$). Quadrupole and sextupole field harmonics (b_1/b_0 and b_2/b_0) are evaluated at a radius of 4 mm. They generate 1st and 2nd order x-dispersion.*

Name	Quantity	Roll (mrad)	Δx offset (μm)	Δy offset (μm)	$\Delta x_{\rm rms}$ vibrate (μm)	$\Delta y_{\rm rms}$ vibrate (μm)	$\Delta B/B_0$ (%)	b_2/b_1 (%)
QF	69	1.12	920	230	2.3	0.58	0.9	10
QD	68	1.10	2930	100	7.3	0.25	4.8	120

Table 5-11. *BC2 arc quadrupole magnet single element tolerances for 8% emittance growth each ($\gamma\varepsilon_{x0} = 3\times10^{-6}$ m, $\gamma\varepsilon_{y0} = 3\times10^{-8}$ m, $\sigma_\delta = 0.25\%$). Sextupole field component tolerances (b_2/b_1) are evaluated at a radius of 4 mm and are very loose for the QDs (120%).*

Name	Quantity	Roll (mrad)	Δx offset (μm)	Δy offset (μm)	$\Delta x_{\rm rms}$ vibrate (μm)	$\Delta y_{\rm rms}$ vibrate (μm)	$\Delta B/B_0$ (%)
SF	68	325	800	160	800	160	>50
SD	68	325	1740	86	1740	86	>50

Table 5-12. *BC2 arc sextupole magnet single element tolerances for 8% emittance growth each ($\gamma\varepsilon_{x0} = 3\times10^{-6}$ m, $\gamma\varepsilon_{y0} = 3\times10^{-8}$ m, $\sigma_\delta = 0.25\%$). The field regulation and roll tolerances are not important (for aligned sextupoles) because the chromaticity of the arc is insignificant.*

180° Arc Section

In order to estimate the dispersion correction range needed we first examine the single element tolerances for the arc. These tolerances are then scaled to estimate the emittance dilution associated with an achievable set of alignment and quadrupole gradient tolerances. This estimated emittance dilution is used to choose the necessary correction range and the scheme is tested for induced non-linear aberrations. The single element tolerances for the 180° arc FODO magnets are listed below in Table 5-10 (dipoles), 5-11 (quadrupoles), and 5-12 (sextupoles). Each tolerance represents a 2% luminosity loss for that single element's effect on one beam (8% emittance increase for one beam in one plane). The effects of these errors increase the IP beam size except for dipole field regulation and quadrupole transverse vibration which steer the beams out of collision. In this case, the betatron phase to the IP is not calculated so phase averaging is applied.

The important vertical emittance dilution mechanisms include vertical misalignments of the quadrupoles and sextupoles and roll errors of quadrupoles and dipoles. Horizontal dilution mechanisms include horizontal misalignments and gradient errors of the QF quadrupoles. The magnetic multipole tolerances in the tables, when scaled down by $\sqrt{N}$, are easily achievable, as are the horizontal alignment and gradient errors of the QD quadrupoles and the roll and field errors of the sextupoles. Static field strength errors of the dipoles can be encompassed in the horizontal alignment of

Rms magnet roll angles	Rms vertical misalignments	Rms horizontal misalignments	Rms static gradient errors	$\Delta\varepsilon_y/\varepsilon_{y0}$	$\Delta\varepsilon_x/\varepsilon_{x0}$
0.5 mrad QF/QD/BB	100 μm QF/QD 60 μm SF/SD	200 μm QF/QD 200 μm SF/SD	0.5% QF/QD	—	—
68 QDs				1.1	$\sim$0
69 QFs				1.1	$\sim$0
138 BBs				0.1	$\sim$0
	68 QDs			5.4	0
	69 QFs			1.0	0
	68 SDs			2.6	$\sim$0
	68 SFs			0.8	$\sim$0
		68 SDs		0	0.1
		68 SFs		0	0.3
		68 QDs		0	$\sim$0
		68 QFs		0	0.2
			68 QDs	$\sim$0	0.1
			69 QFs	$\sim$0	1.7
			Total Expected Dilution *without* Tuning =	12.1	2.4

Table 5-13. *Chosen set of rms alignment tolerances and quadrupole static gradient tolerances for the BC2 arc and their impact on emittance dilution for each plane ($\gamma\varepsilon_{x0} = 3\times10^{-6}$ m, $\gamma\varepsilon_{y0} = 3\times10^{-8}$ m, $\sigma_\delta = 0.25\%$). Vertical alignment of SDs and QDs is most critical.*

the quadrupoles. Regulation and vibration tolerances are not addressed by the tuning schemes discussed here. These non-static problems will need to be corrected by orbit feedback systems or, as in the case of dipole field regulation, all dipoles or groups of dipoles will be powered in series to significantly loosen these tolerances. An achievable set of alignment and quadrupole gradient tolerances is now chosen and the associated emittance dilution is tabulated for each mechanism in Table 5-13.

For these tolerances, the total emittance dilution factor for the vertical plane may be $\sim$12, whereas the horizontal may be $\sim$2. Dispersion correctors should handle at least this range and should also not affect beta functions or introduce betatron coupling. The quadrupole roll tolerances of 0.5 mr and sextupole vertical alignment tolerances of 60 μm were chosen so that cross-plane coupling will not be a problem and therefore no betatron-coupling correction is required (*i.e.*, for a monochromatic beam, 69 QF and 68 QD magnets with 0.5 mr rms roll errors plus 68 SF and 68 SD magnets with 60 μm rms vertical misalignments will produce a 2% luminosity loss for the one beam due to betatron coupling). The sextupoles may easily be beam-based aligned if vertical movers are included with ±1 mm range. If an SD's pole-tip field is temporarily raised to -4 kGauss (from -3 kGauss) and its vertical position is scanned in $\sim$5 steps over the range ±1 mm while the horizontal beam centroid offset is recorded on a $<$4-μm resolution BPM near the next QF, then each sextupole may be aligned to $<$60-μm resolution. This resolution may be improved by using more than one BPM. Note that energy jitter will vary the BPMs reading due to the $\sim$100-mm x-dispersion there. However, all arc x-BPMs may be used together to correct the data for this energy jitter down to $\delta E/E_0 = (4\,\mu\text{m}/\sqrt{68})/(100\,\text{mm}) \sim 5\times10^{-6}$. Figure 5-23 shows a simulated sextupole (SD) alignment scan using one 4-μm resolution x-BPM.

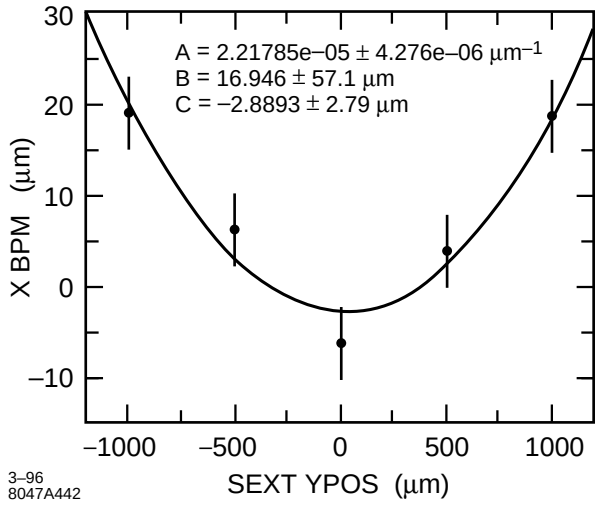

Figure 5-23. *Simulated sextupole (SD) alignment scan using one 4-μm-resolution x-BPM located at the next QF. The SD's pole-tip field is set to -4 kGauss (from -3 kGauss) for the alignment.*

Dispersion Correctors for the Arc. Vertical dispersion correction at the end of the arc can be provided by adding four small skew quadrupoles (of zero nominal field)—one per cell in the last four cells (cells 65–68). This scheme takes advantage of the 90° vertical phase advance per cell by pairing skew quadrupoles at $-I$ transfer matrix (2 cell) separation so that, for equal and opposite skew quadrupole settings, no betatron cross-plane coupling is generated. The two asymmetrically powered pairs of skew quadrupoles are shifted by one cell ($\Delta\psi_y = 90°$) with respect to each other so that both betatron phases are correctable (η_y and η'_y). Betatron coupling is also correctable, if necessary, if one skew quadrupole is also added to each of cells 61–64. In this way four symmetric pairs may be formed (61/63, 62/64, 65/67 and 66/68) which correct betatron coupling without introducing vertical dispersion so that, given the unequal x and y tunes of the arc, all four cross plane correlations are removable within skew quadrupole field limits (not possible for $\Delta\psi_x = 90°$/cell). The range of vertical dispersion correction for one pair of 10-cm-long, ± 1 kGauss pole-tip field, 30-mm pole-tip radius skew quadrupoles located 10-cm upstream of the QD at $\beta_y = 6.5$ m, $\eta_x = 50$ mm is $\Delta\varepsilon_y/\varepsilon_{y0} \sim 12$ at 0.25% rms energy spread for $\gamma\varepsilon_{y0} = 3 \times 10^{-8}$ m (or the peak vertical dispersion induced at the center of the next QD magnet is as much as ± 7 mm per pair). No significant coupling or beta beat is generated over this range. For betatron coupling, one of the four symmetric pairs of skew quadrupoles at $\pm$2-kGauss pole-tip field will correct a 50% vertical emittance dilution due to coupling. These four coupling correctors may be easily added if betatron coupling becomes a problem. Their inclusion will effectively loosen sextupole vertical alignment tolerances by nearly a factor of 2. Of course the skew quadrupoles may also be replaced, with some loss in correction speed, by QD roll-movers with $\pm$10-mr range or SD vertical movers of $\pm$1-mm range (SD vertical mover steering in the x-plane, is small and can be removed with a post-arc launch feedback system); the magnet movers planned exceed these ranges.

The horizontal dispersion may similarly be controlled by adding two pairs of small normal quadrupoles (of zero nominal field). Due to the nominal 108° horizontal phase advance per cell, these quad pairs must be spaced by 5 cells in order to provide a $-I$ separation. It is probably best not to nest the skew and normal correction quads. If cell 54 and 55 as well as cell 59 and 60 include a 10-cm-long, $\pm$2.3-kGauss, 30-mm radius quadrupole which is 10-cm upstream of the QF at $\beta_x = 6.4$ m, $\eta_x = 93$ mm, the emittance correction range per pair will be $\Delta\varepsilon_x/\varepsilon_{x0} = 2.4$ (or the additional horizontal dispersion induced at the center of a QF magnet is as much as ± 28 mm per pair). If cells 56, 57 and 58 also include a 10-cm-long normal quadrupole, then the horizontal dispersion correction scheme will also work for 90°/cell and 135°/cell horizontal phase advance configurations if the appropriate correction quadrupole (CQ) pairs are tuned for a given R_{56} configuration (*i.e.*, $\psi_x = 90°$/cell: CQ pairs 57/59 and 58/60, $\psi_x = 108°$/cell: CQ

Quad type	Quantity	Length (m)	Pole radius (mm)	Max. field (kGauss)	2% lum. step size (kGauss)	$\Delta\eta_{x,y}^{\max}$ at $\beta_{x,y}^{\max}$ (mm)	Max. $\varepsilon_y/\varepsilon_{y0}$
Skew	4–8	0.1	30	$\pm$1.0	$\pm$0.08	7	12
Normal	7	0.1	30	$\pm$2.3	$\pm$0.42	28	2.4

Table 5-14. *BC2 arc dispersion correction magnet specifications for 0.25% rms energy spread, $\gamma\varepsilon_{x0} = 3 \times 10^{-6}$ m and $\gamma\varepsilon_{y0} = 3 \times 10^{-8}$ m. There is one skew quadrupole (or SD vertical mover) in each of the last four (or eight) FODO cells 10-cm upstream of each QD and one normal quadrupole in each of cells 54 through 60, 10-cm upstream of each QF (or QF trim supplies).*

pairs 54/59 and 55/60, $\psi_x = 135°$/cell: CQ pairs 55/59 and 56/60; see Table 5-4). Since the vertical transfer matrix between paired normal quadrupoles (5 cells for 108°/cell) is not $-I$ there will be an insignificant perturbation to the vertical beta function which amounts to a $< 0.2\%$ vertical beta beat amplitude at full horizontal dispersion correction ($\pm$2.3-kGauss quadrupole fields). Of course these CQ quadrupoles may also be replaced by independent QF trim supplies of $\pm$5% range (SF horizontal movers would require a large $\pm$2.5-mm range and may steer too much). The dispersion correction specifications are summarized in Table 5-14.

This scheme of skew and normal quadrupole dispersion correction has been tested over various vertical emittance dilution mechanisms ranging to $\Delta\varepsilon_y/\varepsilon_{y0} \sim 30$. The dispersion was easily corrected with the skew/normal quadrupole pairs and then the arc was tracked with 3000 particles. The emittance dilution was corrected to within 4% without any coupling correction necessary. The remaining 4% dilution was due to betatron coupling which is also correctable as described above. There are also two quadrupoles placed in the dispersion suppressor section at the beginning and end of the arc which can be used to vary the horizontal dispersion function. However, these variable quadrupoles are included to properly match/suppress the arc dispersion function over the various R_{56} configurations (different horizontal phase advance per cell).

Dispersion Measurements. Dispersion correction for the arc can be accomplished in practice by correlating arc and post-arc BPM readings with prelinac energy variations and applying calculated corrections to the skew and normal quadrupole pairs, and/or by switching off the bunch compression rf between the arc and chicane (so that chicane dispersion errors are minimized), then minimizing the measured emittance on the post-chicane wire scanners using simple orthogonal combinations of the dispersion correction quadrupole pairs.

Beta Matching Corrections for the Arc. There are four matching quadrupoles placed at both entrance and exit of the arc which may be used for empirical beta matching into the post-chicane wire scanner section (with pre-chicane rf switched off to minimize dispersion effects). If the arc dispersion is first matched using the BPM correlation technique described above, then dispersion errors from the arcs should not bias the beta matching process significantly. The tolerance on the beta match into the arc is fairly loose. It can be shown that the synchrotron radiation (SR) emittance increase approximately scales with the amplitude of the incoming beta mismatch.

$$\Delta\varepsilon_{\rm SR} \approx B_{\rm mag}\Delta\varepsilon_{\rm SR-nom.} \tag{5.45}$$

Here $B_{\rm mag}(\geq 1)$ is the beta mismatch amplitude in the horizontal plane and $\Delta\varepsilon_{\rm SR-nom.}(\ll \varepsilon_{x0})$ is the nominal SR emittance increase for a matched incoming beam. A very large mismatch of $B_{\rm mag} = 2(\beta_x \approx 4\beta_{x0}, \alpha_x = \alpha_{x0} = 0)$ will increase a nominal 2.4% SR emittance increase to 4.8%. The vertical match has no such constraint.

Name	Quantity	Length (m)	Roll (mrad)	$\Delta B/B_0$ (10^{-5})	b_1/b_0 (10^{-4})	b_2/b_0 (10^{-3})
B1	2	10	0.14	2.1	33.5	377.0
B2	2	10	0.18	2.6	2.8	2.1

Table 5-15. *BC2 chicane dipole single element tolerances for 8% emittance growth each ($\gamma\varepsilon_{x0} = 3 \times 10^{-6}$ m, $\gamma\varepsilon_{y0} = 3 \times 10^{-8}$ m, $\sigma_\delta = 1.5\%$). Quadrupole and sextupole field harmonics (b_1/b_0 and b_2/b_0) are evaluated at a radius of 100 mm. They generate 1st and 2nd order dispersion.*

Steering Correctors for the Arc. Horizontal and vertical dipole correctors at each QF and QD, respectively, will be required (depending on the availability of quadrupole movers) to initially steer the beam line and to use in fast feedback applications. Correctors with $\pm$0.4-kGauss fields and 10-cm length will be adequate to displace the beam nearly $\pm$1 mm at the next similar quadrupole. The horizontal correctors will then need to regulate at $\sim 5 \times 10^{-4}$ over the 100-ms (10 pulse) range while similar vertical correctors will need $\sim 4 \times 10^{-5}$ regulation ($\sim$0.5% luminosity loss due to all correctors in both arcs for both planes). Quadrupole movers will be used to realize the vertical alignment tolerances using beam based alignment techniques.

Chicane Section

As in the BC2 arc, the chicane presents mostly a dispersion correction problem. Since the chicane includes no quadrupoles at dispersion points, emittance dilution mechanisms will include dipole magnet roll errors and dipole field quality effects. Dipole roll errors should be correctable with vertical steering. Table 5-15 shows the approximate single element tolerances (2% luminosity reduction per error per beam) for the two chicane dipole locations; two B1 dipoles at chicane start/end and the two B2 dipoles at chicane center.

If these tolerances are not met, small correction quadrupoles and skew quadrupoles at the half-way point of the B1 dipoles (split at $\eta_x = 40$ mm, $\beta_{x,y} = 50$ m) can be added to control horizontal and vertical dispersion. These quadrupoles would need to be $\sim$10 cm in length, with $\sim$50-mm radius and $\pm$1-kGauss fields. Both dispersion phases can be handled by placing these correctors at the first and last B1 chicane dipole centers which are separated by $\sim \pi/2$ in phase. Betatron coupling and beta-mismatch effects will not be significantly generated due to the large dispersion here (*i.e.*, $\{\eta_x\sigma_\delta\}^2/\beta_x\varepsilon_x \sim 50$). If the sextupole field harmonic tolerances are not met, then small tuner normal sextupoles will also need to be included here to correct second order horizontal dispersion.

5.5.4 Space Charge and Coherent Radiation

The space-charge field of the beam is not insignificant when it exits the low-energy and the high-energy bunch compressors. This field can drive coupling resonances and increase the beam emittance or add to the beam halo. However, estimates of these effects indicate that they are small because the beams are rapidly accelerated and the optics has been chosen to avoid the most significant resonance, namely $2\psi_x \approx 2\psi_y$.

The space-charge fields in the bending magnets manifest themselves in a slightly different manner. There have been a few estimates of these effects which can be separated into a centrifugal space charge force (CSCF) and a coherent synchrotron radiation force (CSR). A calculation of the CSCF in bunched beams [Carlsten 1995] shows that this should not be a limitation in the NLC. In contrast, the CSR may be significant. Here, the longitudinal electric field of the coherent synchrotron radiation induces an energy variation along the bunch [Derbenev 1995]; the coherent radiation

field is similar to a longitudinal wakefield except that the field travels faster than the bunch and acts on leading particles rather than a normal wakefield which acts on trailing particles. In the wigglers and chicanes, this field will destroy the achromaticity of the compressors, thereby causing an increase in the horizontal emittance; the effect is not important in the 180° arcs where the dispersion is smaller and bends are shorter.

If we neglect the shielding effects of the vacuum chamber, the induced energy spread is predicted to be roughly [Derbenev 1995]

$$\sigma_\delta \approx 0.2 \frac{N r_0 L_d}{\gamma R^{2/3} \sigma_z^{4/3}} \quad , \tag{5.46}$$

where N is the bunch charge, L_d and R are the bending magnet length and bending radius, and r_0 and γ are the classical electron radius and the relativistic factor.

As stated, this induced energy spread will break the chromatic cancelation of the wiggler or chicane. The increase in the horizontal emittance is roughly [Raubenheimer 1995b]

$$\Delta\gamma\epsilon_x \approx 0.5\alpha^2 \sigma_x \frac{I}{17kA} \left(\frac{R}{\sigma_z}\right)^{1/3} \tag{5.47}$$

where α is the bend angle and I is the bunch current. In both the NLC low- and high-energy compressors, this predicts roughly 5% horizontal emittance growth.

Finally, the long-wavelength radiation is suppressed by boundary conditions imposed by the vacuum chamber. The point where shielding becomes important can be estimated as:

$$\sigma_z \gtrsim \sqrt{\frac{h^2 w}{\pi^2 R}} \tag{5.48}$$

where h and w are the full height and width of the chamber and R is the bending radius. In the low- and high-energy bunch compressors, we find that shielding is important for bunch lengths greater than 500 μm and 150 μm, respectively. These values are close to the fully-compressed bunch lengths and thus the chamber shielding may reduce the predicted emittance dilution.

At this time, this emittance dilution has not been observed experimentally and thus there is some uncertainty in the calculations. Regardless, it does not appear that the coherent radiation will be a significant limitation to the NLC compressors. It should be noted that this might be one reason not to consider a single stage compressor as the predicted dilution becomes much more important.

5.5.5 Ion Effects

At the start of the prelinac, all ions created by the beam are stably trapped within a single bunch train, except for hydrogen ions which are over-focused between bunches. An upper limit on the critical ion mass is obtained for the maximum current of 90 bunches with 1.5×10^{10} particles each. In this case the critical ion mass is six proton masses at the start and 29 at the end of the prelinac.

The ions will, first, increase the rate of filamentation, due to the additional focusing experienced by the trailing bunches, and, second, cause a nonlinear octupole-like coupling of horizontal and vertical betatron motion [Raubenheimer 1992]. At a pressure of 10^{-8} Torr, the focusing along the bunch train varies by $\Delta Q_y \approx 10^{-4}$ m^{-1} assuming 90 bunches of 1.5×10^{10} particles each. To attain an additional filamentation due to ions which is comparable to that caused by the intrinsic energy spread, a pressure of less than 10^{-9} Torr has to be achieved. Finally, a separation of the horizontal and vertical phase advances by about 5% effectively eliminates the effect of nonlinear coupling.

As in the damping rings and main linacs, the ionization of the residual gas may give rise to a transverse multibunch instability of the electron bunch train in the prelinac. At a pressure of 10^{-8} Torr, the estimated growth time τ_{asym} of this instability is about 90 ns [Raubenheimer 1995a], assuming 90 bunches of 1.5×10^{10} particles each and ignoring decoherence of the ion oscillations. The ion-driven instability causes an increase of the Fourier component at the ion-oscillation frequency of the vertical bunch positions. Traversing the 500-m-long prelinac at a pressure of 10^{-8} Torr amplifies an initial bunch-to-bunch displacement at this Fourier component, characterized by an action value J_{y0}, by a factor 3×10^4. As an example, if the original perturbation is due to the finite number of electrons in the train, the initial action value is about $J_{y0} \approx \sigma_y^2/(2\beta_y N_b n_b) \approx 3 \times 10^{-24}$ m-rad, which yields a negligible emittance growth of $\Delta(\gamma\epsilon_y) \approx 2 \times 10^{-15}$ m-rad.

However, assuming that the initial perturbation is due to a realistic bunch-to-bunch orbit jitter of about 1% σ_y, the emittance blow-up can be as large as 500%. Fortunately, ion decoherence, due to the variation of the vertical ion oscillation frequency with the horizontal position, increases the rise time of the instability by about a factor of two or three, thereby relieving the pressure tolerance by the same factor [Stupakov 1995].

Taking the decoherence into account, and assuming a partial pressure of 5×10^{-9} Torr of CO, the emittance increase resulting from an initial 1% σ_y harmonic bunch-to-bunch offset at the ion frequency would be about 10%. Because the main constituent of the vacuum is hydrogen, which is not trapped in the beam, this is a relatively loose vacuum requirement.

Until further studies and experiments improve our understanding of the ion-driven instability and possible cures, it is assumed that the required pressure in the prelinac is below 10^{-8} Torr of which more than 70% would be H_2.

5.5.6 Synchrotron Radiation

Incoherent synchrotron radiation in bending and quadrupole magnets may increase the energy spread and, more importantly, dilute the horizontal and (if linear coupling or vertical dispersion is nonzero) the vertical emittance. The total emittance growth in the bunch compressor should be smaller than 5% horizontally, and less than 1–2% vertically. The latter number translates into a tolerance for the tuning procedures and the diagnostics. In addition, the induced energy-spread should be small compared with the original energy spread of the bunch.

The effects of synchrotron radiation in the longitudinal and the horizontal phase space are summarized in Table 5-16 for wiggler, arc, and chicane. In all cases, the number of radiated photons per electron, N_γ, is much larger than one so that the resulting net effect can be described by a Gaussian distribution. The critical energy $E_c \equiv 3\hbar c\gamma^3/(2\rho)$ is only a few keV. Therefore, the radiating particles stay inside the energy acceptance of the system. The average energy loss, ΔE_{rad}, and the additional rms momentum spread due to synchrotron radiation, $\Delta\delta_{\rm rms}$, are both small. The change of the horizontal emittance can be estimated from [Raubenheimer 1994a]

$$\Delta(\gamma\epsilon_x) \approx 4 \cdot 10^{-8} \left(\frac{E}{\text{GeV}}\right)^6 I_5 \tag{5.49}$$

where I_5 denotes the fifth synchrotron radiation integral [Helm 1973]. A mismatch between the synchrotron radiation effects and the original beam distribution can lead to an emittance growth which is larger than predicted by Eq. 5.49 [Spence 1993]. This difference could be especially important for the chicane, since the phase advance over the four bending magnets is only about 90°. To estimate the actual emittance growth, a simulation study has been performed using the computer code MAD [Grote 1990]. The simulations show an emittance growth of approximately $\Delta(\gamma\epsilon_x) \approx 2 \times 10^{-9}$ m-rad in the chicane, which is consistent with the simple estimate of Eq. 5.49, and indicates that the effect of the radiation-lattice mismatch is small. The total increase of the horizontal normalized emittance in the bunch compressor is then about 2.6%. We conclude that the effects of incoherent synchrotron radiation appear insignificant.

	Wiggler	Arc	Chicane
N_γ	99	662	28
E_c (keV)	3.5/4.6	25	7.4
ΔE_{rad} (keV)	134	5300	66
$\Delta\delta_{\rm rms}$ (%)	$1.3 \cdot 10^{-3}$	$4 \cdot 10^{-3}$	$8 \cdot 10^{-5}$
$\Delta(\gamma\epsilon_x)$ (10^{-6} m-rad)	0.039	0.038	0.0015
$\Delta(\epsilon_x)/(\epsilon_{x\,0})$ (%)	1.3	1.3	0.05

Table 5-16. *Effects of synchrotron radiation in wiggler, arc, and chicane.*

5.6 Tolerances

5.6.1 Alignment and Field Tolerances

These are discussed in the text. In general, all transverse alignment and magnet tolerances in the bunch compression system are relatively loose. The only field tolerances that are tight are those in the spin rotator system and the bending magnet multipoles in the chicane. Both of these tolerances are eased using simple tuning techniques similar to those routinely used in the SLC bunch compressors. All of the magnet alignment tolerances are substantially larger than the expected resolution from the beam-based alignment; the alignment techniques are discussed in greater detail in Chapter 7.

5.6.2 Tolerances on RF Phase, Energy, and Intensity

Some of the tightest tolerances in the bunch compressor system are those on the (relative) rf phase stability. The tolerance on the phase difference of electron and positron compressor rf is set by the loss of luminosity when the beams do not collide at the minimum waist position. A collision which is longitudinally offset by $\Delta s = 0.2\beta_y^\star$ leads to a 2% loss of luminosity, which translates into a maximum tolerable rf phase difference $\Delta\phi_{SB,e^+e^-}$ or $\Delta\phi_{LB,e^+e^-}$ between the S-band and L-band rf systems, respectively, on the electron and positron side. This tolerance can be as tight as 0.17° (Table 5-17) and may be difficult to meet because the compressors are located more than 20-km apart.

Even tighter tolerances on relative-phase stability have to be achieved, on either side of the IP, between different compressor and linac rf systems. If the beam is injected into the main linac at a wrong phase, the final beam energy changes. This energy change sets a tolerance on the relative rf phase stability of linac and compressor rf, and on the allowed bunch-to-bunch energy variation due to multibunch beam loading or intensity variation in the various compressor subsystems.

In case the beam is nominally off-crest by an X-band phase angle ϕ_{XB}, the maximum allowed phase error $\Delta\phi_{XB}$ (in degree), which causes a 0.1% average energy change, is given by

$$\Delta\phi_{XB} \leq \frac{10^{-3}\,360}{2\pi\tan\phi_{XB}} \tag{5.50}$$

		NLC-Ia	NLC-Ic	NLC-IIa	NLC-IIc
$E_{\max}$	(GeV)	267	233	534	473
$N_{\rm part}$	(10^{10})	0.65	0.85	0.95	1.25
Final σ_z	(μm)	100	150	125	150
σ_y^*	(nm)	4.52	7.00	3.57	5.35
θ_y^*	(μrad)	36.17	35.02	28.59	26.75
$\Delta\phi_{SB\ e^+e^-}$	(°)	0.17	0.27	0.17	0.27
$\Delta\phi_{LB\ e^+e^-}$	(°)	0.50	0.56	0.44	0.62
$\Delta z_{e^+e^-}$	(μm)	50	80	50	80
ϕ_{XB}	(°)	-14.4	-15.1	-7.2	-11.0
ϕ_{PL}	(°)	-4	-5	-5	-8
$\Delta\phi_{XB}$	(°)	0.22	0.21	0.45	0.30
$\Delta\phi_{SB}$	(°)	0.055	0.053	0.112	0.073
$\Delta\phi_{LB}$	(°)	0.16	0.11	0.29	0.16
$\Delta\phi_{PL}$	(°)	0.32	0.22	0.57	0.33
Δz_{XB}	(μm)	16	15	33	21
Δz_{SB}	(μm)	16	15	33	21
Δz_{LB}	(μm)	95	63	167	96
Δz_{PL}	(μm)	95	63	167	96
$\left.\frac{\Delta E}{E}\right\|_{XB}$	(10^{-3})	1.0	1.0	1.0	1.0
$\left.\frac{\Delta E}{E}\right\|_{SB}$	(10^{-3})	0.45	0.43	0.91	0.59
$\left.\frac{\Delta E}{E}\right\|_{LB}$	(10^{-3})	0.19	0.13	0.33	0.19
$\left.\frac{\Delta E}{E}\right\|_{PL}$	(10^{-3})	4.0	4.7	6.1	5.3
$\frac{\Delta N}{N}_{XB}$	(%)	6.4	4.5	8.1	5.7
$\frac{\Delta N}{N}_{SB}$	(%)	30	21	40	20
$\frac{\Delta N}{N}_{LB}$	(%)	290	148	351	154
$\frac{\Delta N}{N}_{PL}$	(%)	116	105	121	80

Table 5-17. *Tolerances on rf phase, single-bunch energy, and intensity in the various compressor subsystems for four different NLC scenarios, corresponding to either 2% loss of luminosity or to a 0.1% change of average bunch energy, at the end of the main linac. Subindices XB, SB, LB and PL refer to main X-band linac, S-band rf of the second compressor, L-band rf of the first compressor, and the prelinac (S-band rf), respectively.*

and the corresponding longitudinal position error (meter) in main linac and second compressor is

$$\Delta z_{XB} \leq \frac{10^{-3}\,\lambda_{XB}}{2\pi \tan\phi_{XB}} \tag{5.51}$$

where λ_{XB} denotes the wavelength of the X-Band rf (26 mm). The maximum phase error $\Delta\phi_{SB}$ for the S-band rf of the second compressor is equal to

$$\Delta\phi_{SB}\,(^\circ) \leq \frac{\Delta z_{XB}\,360}{\lambda_{SB}}, \tag{5.52}$$

and the maximum single-bunch energy variation due to multi-bunch beam loading in the S-Band rf section is

$$\left.\frac{\Delta E}{E}\right|_{SB} \leq \frac{\Delta z_{XB}}{R^c_{56}} \tag{5.53}$$

The tolerances for the first (L-Band) compressor are obtained in a similar way, taking account of the compression ratio $-R^c_{56}/R^a_{56}$ of the second stage. We thus have

$$\Delta z_{LB} \leq -\frac{\Delta z_{XB}\,R^a_{56}}{R^c_{56}}\quad , \tag{5.54}$$

$$\Delta\phi_{LB}\,(^\circ) \leq \frac{\Delta z_{LB}\,360}{\lambda_{LB}}\quad , \tag{5.55}$$

$$\left.\frac{\Delta E}{E}\right|_{LB} \leq \frac{\Delta z_{LB}}{R^w_{56}}\quad . \tag{5.56}$$

There is also a tolerance on the bunch-to-bunch energy variation in the prelinac. A relative energy error δ_{PL} at the end of the prelinac causes a change of the longitudinal position Δz_{XB} of the bunch center at the exit of the second compressor, which in lowest order is given by

$$\Delta z_{XB} \approx \frac{1}{2} f_{2,c} k_{2,c} {R^a_{56}}^2 R^c_{56} \delta^2_{PL} + T^c_{566}(-f_{2,c}R^a_{56}+1)^2\delta^2_{PL} + \mathcal{O}(\delta^3_{PL}) \tag{5.57}$$

from which the maximum allowed energy variation $\Delta E/E|_{PL} \equiv \delta_{PL,\,max}$ in the prelinac can be estimated:

$$\left.\frac{\Delta E}{E}\right|_{PL} \leq \frac{3}{4}\left[\frac{\Delta z_{XB}}{\frac{1}{2} f_{2,c} k_{2,c} {R^a_{56}}^2 R^c_{56} + T^c_{566}(-f_{2,c}R^a_{56}+1)^2}\right]^{\frac{1}{2}} \tag{5.58}$$

where the factor $3/4$ in front is an empirical correction due to finite bunch length and higher-order contributions.

A phase error in the prelinac causes both an energy error at the exit of the prelinac and a phase error in the main linac. Both these effects lead to a change of the final energy, but the latter effect is ten times as severe as the former. For this reason, the energy error at the end of the prelinac may be ignored, and the tolerance on the longitudinal position in the prelinac is the same as that for the L-Band compressor, while the phase tolerance (in degree S-Band) is simply twice that of the L-Band rf.

A limit on single-bunch intensity variation arises from the above tolerances on energy and from the single-bunch beam loading. Denoting the relative energy change per 10^{10} particles due to longitudinal wakefields by δ_{10}, the intensity tolerance for an rf section may be written as

$$\frac{\Delta N}{N} \leq \frac{\Delta E}{E}\cdot\frac{10^{10}}{\delta_{10}\,N}, \tag{5.59}$$

where $\Delta E/E$ designates the allowed energy variation.

		NLC-Ia	NLC-Ic	NLC-IIa	NLC-IIc
$\Delta\phi_{c,\,BC2}$	(°)	0.76	0.56	1.06	0.53
$\Delta\phi_{c,\,BC1}$	(°)	0.81	0.42	0.99	0.44
$\Delta\phi_{c,\,PL}$	(°)	0.17	0.20	0.26	0.23
$\Delta f\|_{c,\,BC2}$	(kHz)	17	12	23	12
$\Delta f\|_{c,\,BC1}$	(kHz)	18	9	22	10
$\Delta f\|_{c,\,PL}$	(kHz)	3.7	4.5	5.7	5.0

Table 5-18. *Tolerances on phase and frequency stability for the additional rf systems which are employed to compensate multibunch beam loading, considering four different NLC scenarios. Tolerances correspond to a 0.1% change of average bunch energy, at the end of the main linac. Subindices $BC2$, $BC1$, and PL refer to the second compressor, first compressor, and prelinac, respectively. The subindex `c' indicates the compensating nature of the rf.*

Finally, if the ΔF beam loading compensation is used in either of the two compressor stages or the prelinac, then there are two additional rf systems which are used for multibunch beam loading compensation. The tolerance on the phase stability for these rf systems follows directly from the tolerable energy error ΔE in the pertinent compressor subsystem:

$$\Delta\phi_{mbc} \leq \Delta E / V_{mbc} \tag{5.60}$$

where V_{mbc} is the amplitude of the compensating rf voltage. The limit on the energy deviation, ΔE, is taken from Eqs. 5.53, 5.56 or 5.58, respectively. Similarly, the allowed frequency error for the compensating rf is determined by the corresponding phase (or energy) error at the end of the bunch train, *i.e.*,

$$\frac{\Delta f}{f} \leq \frac{c\,\Delta E}{2\pi V_{mbc} l_{\rm train} f} \quad . \tag{5.61}$$

Table 5-17 compiles tolerances on main rf and T_{566}-compensating rf for all compressor subsystems and four different NLC scenarios. Some tolerances shown in the table are easy to achieve, for instance those on the intensity. Other tolerances may need more attention. For example, the phase-stability tolerance for the second compressor is less than a tenth of a degree S-Band.

Table 5-18 lists tolerances on phase and frequency stability for the three double rf systems which compensate for multibunch beam loading in the different compressor subsystems. In this case, the tolerances are tightest for the prelinac, where a phase stability of about 0.2° S-band needs to be achieved. By comparison, the phase tolerances for the compensating rf of the two compressor stages are at least 0.4° S-band. They are, thus, looser than those of the corresponding main rf systems.

5.7 Conclusions and Comments

A design of a two-stage bunch compressor has been described that meets all specifications, as far as single- and multibunch dynamics is concerned. The bunch compressor has been designed in view of NLC-I and NLC-II, *i.e.,* for a c.m. energy of 0.5 and 1 TeV, and may have to be reevaluated once a specific operating range for NLC-III, with 1.5 TeV-c.m. energy, is determined.

Possible topics of further study in the bunch-compressor design are the following: First, if attempts are successful to correct the synchronous phase variation in the damping rings, the bunch compressor may be simplified and shortened. Second, a final value has to be chosen for the $R_{56}^{a,c}$ matrix elements of arc and chicane. A reduction of the present values would reduce the (significant) length of the rf system in the second compressor, at the expense of increased sensitivity to the incoming beam conditions. In particular, the choice of $R_{56}^{a,c}$ depends, of course, on the assumed initial phase variation. Third, the possibility of and schemes for bunch shaping need to be explored. Also, the design of two 90° compressor stages as an alternative to the present "90°/360°" scheme could be investigated. Next, one or both compressor stages may be redesigned so as to reduce the T_{566}-matrix elements. This would improve the performance in the longitudinal phase space, and could also reduce the length of the bunch compressor.

As a final point, we note that a single-stage compressor remains the most attractive alternative to the present design. A single stage would be shorter, easier to tune, and would improve the longitudinal dynamics at high intensity. The main disadvantage is that the nonlinearities in the longitudinal phase space are more severe, because of the much larger energy spread. Consequently, for a single stage, the T_{566}-matrix element has to be reduced to about a third of the R_{56}-matrix element. The residual nonlinearity can then be compensated by a decelerating rf as in the double-stage scheme. A small T_{566}-matrix element may be realized by placing quadrupoles at dispersive locations and/or by adding sextupoles. In reducing the T_{566}, care has to be taken, since the emittance dilution in the transverse phase space has to remain acceptable for an rms energy spread as large as 5%. So far, attempts to design a single-stage compressor with satisfactory performance in all phase-space dimensions have not been successful. Nevertheless, this option should be pursued further.

References

[Bane] The program LITRACK for simulating longitudinal wakefield effects in linear accelerators has been written by K. Bane.

[Bane 1995] K. Bane, "The Short-Range Wake Field for the NLC X-Band Structure", NLC–Note–9 (1995).

[Brown 1977] K. Brown, F. Rothacker, D. Carey, C. Iselin, "TRANSPORT – A Computer Program for Designing Charged Particle Beam Transport Systems", SLAC–91 (1977).

[Brown 1980] K.L. Brown *et al.*, CERN 80-04, (March 1980).

[Burke 1995] D. Burke, "Proposal for New NLC Operating Plane", SLAC memorandum, unpublished (1995).

[Carlsten 1995] B.E. Carlsten and T.O. Raubenheimer, "Emittance Growth of Bunched Beams in Bends," *Phys. Rev. E* **51**:1453 (1995).

[Delahaye 1985] J.P. Delahaye and J. Jäger, "Variation of the Dispersion Function, Momentum Compaction Factor and Damping Partition Numbers with Particle Energy Deviation", *Particle Accelerators* **18**, 183 (1986).

[Derbenev 1995] Y.S. Derbenev, J. Rossbach, E.L. Saldin, V.D. Shiltsev, "Microbunch Radiative Tail-Head Interaction", (DESY) TESLA–FEL 95–05 (1995).

[Emma 1994] P. Emma, "A Spin Rotator System for the NLC", NLC–Note–7 (1994).

[Emma 1995] P. Emma, "A Skew Correction and Diagnostic Section for Linear Colliders", in preparation (1995).

[Fieguth 1987] T. Fieguth, "Snakes, Rotators, Serpents and the Octahedral Group", SLAC–PUB–4195 (January, 1987).

[Fieguth 1989] T.H. Fieguth, "The Optical Design of the Spin Manipulation System for the SLAC Linear Collider", *Proc. of the 1989 Part. Acc. Conf.*, Chicago, IL (1989).

[Grote 1990] H. Grote and F. C. Iselin, *The MAD Program, Version 8.1, User's Reference Manual*, CERN/SL/**90-13** (AP) (1990).

[Helm 1973] R.H. Helm, M.J. Lee and P.L. Morton, M. Sands, "Evaluation of Synchrotron Radiation Integrals", *Proc. of the 1973 Part. Acc. Conf.*, San Francisco, CA; *IEEE Trans. Nucl. Sci.* NS–20, **3**, 900 (1973).

[Kikuchi 1992] M. Kikuchi, "Multi-Bunch Energy Compensation in Bunch Compressor of Linear Colliders", *Proc. of the 1992 High Energy Acc. Conf.*, Hamburg, Germany, 864 (1992).

[Miller 1995] R. Miller, private communication (1995).

[Oide 1994] K. Oide, discussed at XLC miniworkshop, SLAC, Dec. 1994 (1994).

[Palmer 1990] R. Palmer, "Prospects for High-Energy e^+e^- Linear Colliders", *Ann. Rev. Nucl. Part. Sci.* **40**, 529–592 (1990).

[Raubenheimer 1992] T.O. Raubenheimer and P. Chen, "Ions in the Linacs of Future Linear Colliders", *Proc. of LINAC 92*, Ottawa, Canada (1992).

[Raubenheimer 1993] T.O. Raubenheimer, P. Emma, S. Kheifets, “Chicane and Wiggler Based Bunch Compressors for Future Linear Colliders”, *Proc. of the 1993 Part. Acc. Conf.*, Washington, DC (1993).

[Raubenheimer 1994a] T.O. Raubenheimer, “Bunch Compressor Parameters”, NLC–NOTE–2 (1994).

[Raubenheimer 1994b] T.0. Raubenheimer, private communication (1994).

[Raubenheimer 1995a] T.O. Raubenheimer and F. Zimmermann, “A Fast Beam-Ion Instability: Linear Theory and Simulations”, *Phys. Rev. E* **52**, 5487 (1995).

[Raubenheimer 1995b] T.O. Raubenheimer, “Summary of the Linac Working Group”, Proc. of the MicroBunches Workshop, Brookhaven, NY (1995).

[Rogers 1991] R. Rogers and S. Kheifets, “Misalignment Study of the NLC Bunch Compressor”, Proc. of the 1991 IEEE Part. Acc. Conf., San Francisco, CA (1991).

[Spence 1991] W. Spence, private communication (1991).

[Spence 1993] W. Spence, “Phase Space and Synchrotron Radiation in High Energy Electron Transport Lines”, *Proc. of the Emittance 93 Workshop*, KEK **93-13** 362 (1993).

[Stupakov 1995] G. Stupakov, T.O. Raubenheimer and F. Zimmermann, “A Fast Beam-Ion Instability: Effect of Ion Decoherence”, *Phys. Rev. E* **52**, 5499 (1996).

[Woodley 1994] M. Woodley, private communication (1994).

[Zimmermann 1994] F. Zimmermann, “Longitudinal Single-Bunch Dynamics and Synchrotron Radiations Effects in the Bunch Compressor”, NLC–Note–3 (October 1994).

Contributors

- Paul Emma
- Zenghai Li
- Tor Raubenheimer
- Kathy Thompson
- Frank Zimmermann